The Astrophysical Journal Supplement Series, 284:64 (17pp), 2026 June https://doi.org/10.3847/1538-4365/ae6777

The NIRISS PASSAGE Spectroscopic Redshift Catalog in COSMOS

Mason S. Huberty[1], Kalina V. Nedkova[2,3,4], Zahra Sattari[2], Vihang Mehta[2], Claudia Scarlata[1], Marc Rafelski[3,4], Matthew J. Hayes[5], Peter J. Watson[6], Ayan Acharyya[6], Jacob Levine[7], Benedetta Vulcani[6], Alexandra Le Reste[1], Farhanul Hasan[4], James Colbert[2], Michele Trenti[8,9], Xin Wang[10,11,12], Axel Runnholm[5], Matthew A. Malkan[7], Andrew J. Bunker[13], Anahita Alavi[2], Hakim Atek[14], Andrew J. Battisti[15,16], Y. Sophia Dai[17], Keunho Kim[2], Alaina Henry[4], Michael J. Rutkowski[18], Hollis Akins[19], Caitlin M. Casey[19,20,21], Maximilien Franco[22], Santosh Harish[23], Jeyhan S. Kartaltepe[23], Anton Koekemoer[4], Daizhong Liu[24], Henry McCracken[25], Jason Rhodes[26], Brant Robertson[27], and Marko Shuntov[21,28]

[1] Minnesota Institute for Astrophysics, University of Minnesota, Twin Cities, 116 Church St SE, Minneapolis, MN 55455, USA; huber458@umn.edu
[2] IPAC, California Institute of Technology, 1200 E. California Blvd, Pasadena, CA 91125, USA
[3] Department of Physics and Astronomy, Johns Hopkins University, 3400 North Charles Street, Baltimore, MD 21218, USA
[4] Space Telescope Science Institute, 3700 San Martin Drive, Baltimore, MD 21218, USA
[5] Department of Astronomy, Stockholm University, AlbaNova University Center, SE-106 91 Stockholm, Sweden
[6] INAF, Osservatorio Astronomico di Padova, Vicolo dell'Osservatorio 5, 35122 Padova, Italy
[7] Department of Physics and Astronomy, University of California, Los Angeles, 430 Portola Plaza, Los Angeles, CA 90095, USA
[8] School of Physics, University of Melbourne, Parkville, VIC 3010, Australia
[9] ARC Centre of Excellence for All Sky Astrophysics in 3 Dimensions (ASTRO 3D), Australia
[10] School of Astronomy and Space Science, University of Chinese Academy of Sciences (UCAS), Beijing 100049, People's Republic of China
[11] National Astronomical Observatories, Chinese Academy of Sciences, Beijing 100101, People's Republic of China
[12] Institute for Frontiers in Astronomy and Astrophysics, Beijing Normal University, Beijing 102206, People's Republic of China
[13] Department of Physics, University of Oxford, Keble Road, Oxford, OX1 3RH, UK
[14] CNRS, Institut d'Astrophysique de Paris, 98 bis Boulevard Arago, 75014 Paris, France
[15] International Centre for Radio Astronomy Research, University of Western Australia, 7 Fairway, Crawley, WA 6009, Australia
[16] Research School of Astronomy and Astrophysics, Australian National University, Cotter Road, Weston Creek, ACT 2611, Australia
[17] Chinese Academy of Sciences South America Center for Astronomy (CASSACA), National Astronomical Observatories(NAOC), 20A Datun Road, Beijing 100012, People's Republic of China
[18] Department of Physics and Astronomy, Minnesota State University, Mankato, 141 Trafton Science Center N, Mankato, MN 56001, USA
[19] Department of Physics, University of California, Santa Barbara, Santa Barbara, CA 93106, USA
[20] The University of Texas at Austin, 2515 Speedway Blvd Stop C1400, Austin, TX 78712, USA
[21] Cosmic Dawn Center (DAWN), Denmark
[22] Université Paris-Saclay, Université Paris Cité, CEA, CNRS, AIM, 91191, Gif-sur-Yvette, France
[23] Laboratory for Multiwavelength Astrophysics, School of Physics and Astronomy, Rochester Institute of Technology, 84 Lomb Memorial Drive, Rochester, NY 14623, USA
[24] Purple Mountain Observatory, Chinese Academy of Sciences, 10 Yuanhua Road, Nanjing 210023, People's Republic of China
[25] Institut d'Astrophysique de Paris, UMR 7095, CNRS, and Sorbonne Université, 98 bis boulevard Arago, F-75014 Paris, France
[26] Jet Propulsion Laboratory, California Institute of Technology, 4800 Oak Grove Drive, Pasadena, CA 91001, USA
[27] Department of Astronomy and Astrophysics, University of California, Santa Cruz, 1156 High Street, Santa Cruz, CA 95064, USA
[28] Niels Bohr Institute, University of Copenhagen, Jagtvej 128, DK-2200, Copenhagen, Denmark
Received 2026 January 5; revised 2026 April 2; accepted 2026 April 28; published 2026 June 2

Abstract

We present the Parallel Application of Slitless Spectroscopy to Analyze Galaxy Evolution (PASSAGE) spectroscopic redshift catalog in the COSMOS field. PASSAGE is a JWST Cycle 1 Near Infrared Imager and Slitless Spectrograph (or NIRISS) wide-field slitless spectroscopy pure-parallel survey, obtaining near-infrared spectra of thousands of extragalactic sources. Fifteen out of 63 PASSAGE fields fall within the Hubble Space Telescope COSMOS footprint, of which 11 overlap with COSMOS-Web, a JWST treasury survey providing additional space-based photometry. We present our custom line-finding algorithm and visual inspection effort used to identify emission lines and derive the spectroscopic redshifts for line-emitting sources in PASSAGE. The line-finding algorithm identifies between ∼200 and 950 line-emitting candidates per field, of which typically 47% were identified as true emission lines post visual inspection. We identify 2183 emission-line sources at $0.08 \lesssim z \lesssim 4.7$, 1896 of which have available COSMOS photometric redshifts. We find excellent redshift agreement between the COSMOS photometric redshifts and the PASSAGE spectroscopic redshifts for strong (signal-to-noise ratio > 5), multi-line-emitting sources. This agreement weakens for PASSAGE single-line emitters with ambiguous identities. These single-line emitters are likely misidentified around 18% of the time based on comparisons to photometric redshifts. We derive stellar masses using PASSAGE photometry and spectroscopic redshifts, in broad agreement with existing COSMOS-Web stellar masses, but with some discrepancy driven by redshift disagreements. We publicly release this spectroscopic redshift catalog, which will enable community-led science in prime extragalactic fields and serve as a crucial dataset for validating Euclid and Roman spectroscopy.

Unified Astronomy Thesaurus concepts: Galaxy spectroscopy (2171); Spectroscopy (1558); Near infrared astronomy (1093); Redshift surveys (1378)

Materials only available in the online version of record: machine-readable table

1. Introduction

The James Webb Space Telescope (JWST) has opened up a new parameter space in the study of galaxy evolution. JWST's wide-field slitless spectroscopy (WFSS) observations provide unbiased observations of thousands of sources simultaneously by obtaining spectra for all objects in the field of view without target preselection. The unparalleled sensitivity of JWST in the near-infrared (NIR) permits the detection of faint emission lines for both known and new extragalactic sources. Galaxies in the mid- to low-mass regime ($\log[M_*/M_\odot] \lesssim 10$) are of particular interest, as they represent a larger share of the galaxy population than their massive counterparts—yet prior to JWST, they could not be reliably characterized at moderate to high redshifts. Optical emission lines such as the Balmer lines, [O III] 4960, 5008 Å, and [O II] 3727, 3730 Å from sources at $1 \lesssim z \lesssim 4$ fall in the NIR regime, alongside [S III] 9069, 9532 Å and Paschen lines at the lowest redshifts ($z < 1$). These lines can be used to very precisely constrain the redshift of their hosts and enable measurements of their physical properties. JWST WFSS surveys have already proved fruitful, providing insights into the baryon cycle, reionization and the early Universe, dwarf galaxy physical properties, large-scale structure, and active galactic nuclei (AGN), as demonstrated by surveys such as EIGER (D. Kashino et al. 2023), FRESCO (P. A. Oesch et al. 2023), CEERS (S. L. Finkelstein et al. 2025), CANUCS (G. T. E. Sarrouh et al. 2026), and GLASS (T. Treu et al. 2022; P. J. Watson et al. 2025a).

The Near Infrared Imager and Slitless Spectrograph (NIRISS) provides WFSS in the NIR wavelength range of ~1 to ~2.2 μm (C. J. Willott et al. 2022). While the modest resolution of NIRISS ($R \sim 150$) may limit the number of spectral features that can be identified, it is well suited for observations of large populations of sources, the identification of strong emission lines, spatially resolved studies (e.g., A. Acharyya et al. 2025; V. Estrada-Carpenter et al. 2025), and high-redshift galaxy detection (e.g., A. Runnholm et al. 2025).

The Parallel Application of Slitless Spectroscopy to Analyze Galaxy Evolution (PASSAGE) survey is a Cycle 1 JWST GO pure-parallel survey utilizing the NIRISS WFSS mode (M. A. Malkan et al. 2025). Owing to its pure-parallel design, the survey has pseudo-random pointings determined by independent JWST primary observations, with NIRISS data collected simultaneously. As a result, the effects of cosmic variance are substantially mitigated, since each PASSAGE field is independent of the others.

That said, a significant number of PASSAGE fields fall within the Cosmic Evolution Survey (COSMOS; N. Scoville et al. 2007) field, as a result of broad observational attention devoted to this region of the sky. COSMOS is a ~2 square degree field with extensive multiwavelength data (N. Scoville et al. 2007), acting as a crucial training field for JWST surveys. Observations of the COSMOS field began with Hubble Space Telescope (HST) Advanced Camera Survey (ACS) F814W (A. M. Koekemoer et al. 2007) and continued with Spitzer Space Telescope mid-infrared imaging (D. B. Sanders et al. 2007), VISTA NIR coverage (H. J. McCracken et al. 2012), Subaru/Supreme Cam imaging (P. Capak et al. 2007; Y. Taniguchi et al. 2015), the Canada–France–Hawaii Telescope program CLAUDS (M. Sawicki et al. 2019), and the Hyper-Supreme Cam Subaru Strategic Program (H. Aihara et al. 2019), leading to the COSMOS2020 catalog (J. R. Weaver et al. 2022). With the launch of JWST, COSMOS2020 was expanded even further to the COSMOS-Web/COSMOS2025 catalog with the addition of JWST NIRCAM (F115W, F150W, F277W, and F444W) and MIRI (F770W) filters (M. Shuntov et al. 2025). This extensive photometric dataset enables well-constrained spectral energy distribution (SED) modeling, yielding robust galaxy properties such as stellar masses, which cannot be reliably derived from the wavelength-limited NIRISS spectroscopic data alone. The COSMOS multiband photometry also enables reliable photometric redshift estimates for many sources in the field. However, these redshifts often carry large uncertainties, making spectroscopic redshifts essential for accurately constraining galaxy distances. Sources in the overlap between PASSAGE and COSMOS therefore benefit from robust spectroscopic redshifts and extensive photometric coverage, together yielding a large, well-constrained sample for studies of galaxy evolution. Although COSMOS already hosts one of the most comprehensive spectroscopic catalogs (see A. A. Khostovan et al. 2026), the majority of previous surveys relied on preselection and are consequently biased toward more massive galaxies. PASSAGE complements these efforts by providing spectroscopic redshifts for lower-mass systems.

In this paper, we present the spectroscopic redshift and stellar-mass catalog for the 15 PASSAGE fields overlapping with COSMOS HST/ACS F814W imaging, including the extensive emission-line-finding effort and visualization tools required for such a study. This paper is structured as follows. In Section 2, we present the PASSAGE sample and data-reduction procedures. In Section 3, we present the emission-line-finding procedure. In Section 4, we present the PASSAGE in COSMOS catalog. We conduct redshift comparisons of the PASSAGE sample to ancillary data in Section 5. We discuss the statistics of the catalog in Section 6. The stellar masses of the sample are discussed in Section 7. Our conclusions are outlined in Section 8.

In this paper, the standard concordance cosmology model ($\Omega_m = 0.3$, $\Omega_\Lambda = 0.7$, $H_0 = 70\,\mathrm{km\,s^{-1}\,Mpc^{-1}}$) and AB magnitude system (J. B. Oke & J. E. Gunn 1983) are used. Forbidden lines are indicated as follows, if presented without wavelength values: [O II] $\lambda\lambda$3727, 3730 = [O II], [Ne III] λ3869 = [Ne III], [O III] λ5008 = [O III], [N II] λ6585 = [N II], and [S II] $\lambda\lambda$6718, 6732 = [S II].

2. The PASSAGE Survey

PASSAGE is a Cycle 1 JWST GO pure-parallel survey that obtained NIRISS imaging and slitless spectroscopy of 63 fields (totaling ~305 square arcminutes; M. A. Malkan et al. 2025).

PASSAGE is characterized by several key features: it is an unbiased spectroscopic survey without photometric preselection; it samples dozens of independent sight lines, mitigating the effects of cosmic variance; it provides continuous NIR coverage over ~1–2.2 μm, capturing rest-frame optical

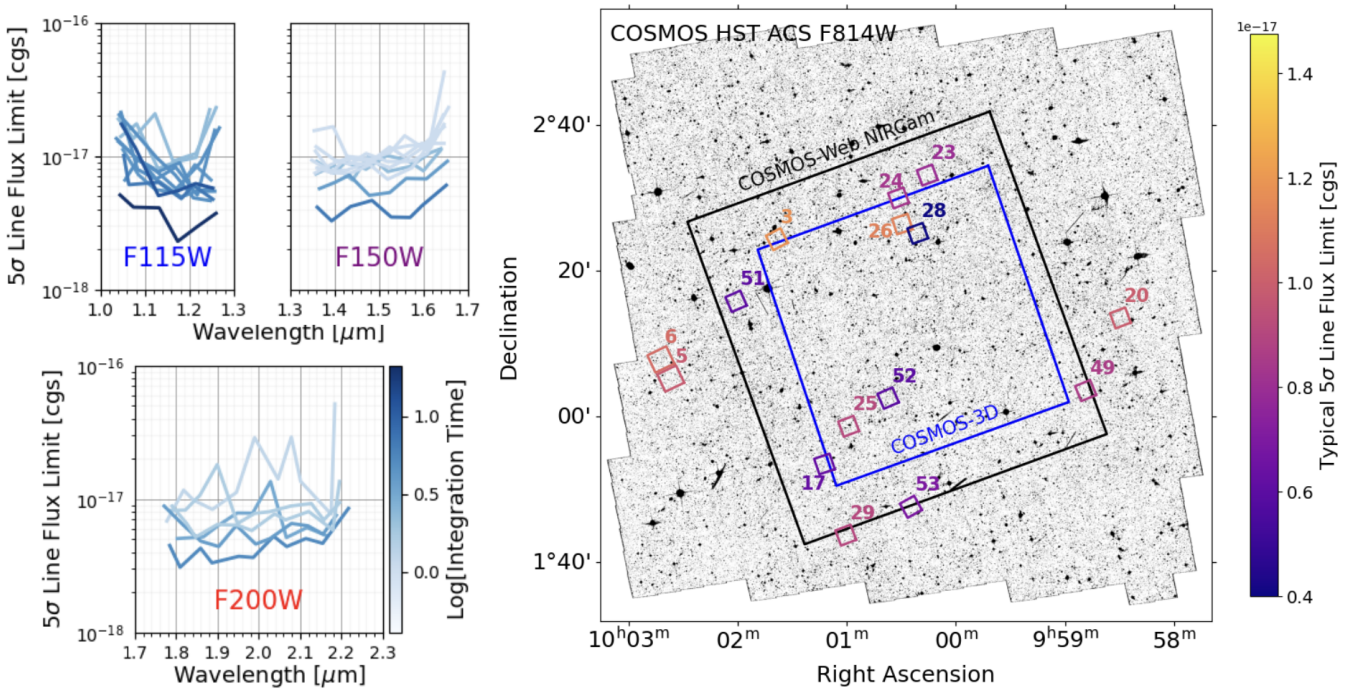

Figure 1. Left panels: typical PASSAGE 5σ detection limits for emission lines in PASSAGE (including both point sources and extended sources), in erg s^{-1} cm^{-2}, for the F115W (upper left), F150W (upper right), and F200W (bottom) filters. The color of each line corresponds to its integration time, with darker colors indicating longer integration times. Right panel: locations of the 15 PASSAGE fields analyzed in this work, shown relative to the footprints of COSMOS HST/ACS imaging (the base of the COSMOS2020 catalog; A. M. Koekemoer et al. 2007; R. Massey et al. 2010), COSMOS-Web (M. Franco et al. 2026), and COSMOS-3D (K. Kakiichi et al. 2024). The color of each field corresponds to its typical 5σ detection limit.

emission lines at cosmic noon; and it combines high spatial resolution (0.″065 per pixel) with up to two orthogonal grism orientations to reduce spectral overlap and contamination. In total, PASSAGE has delivered over 10,000 NIR grism spectra across these fields, enabling statistically robust studies of galaxy evolution across a wide range of environments and redshifts.

The PASSAGE observing strategy is thoroughly discussed in M. A. Malkan et al. (2025), but to briefly summarize: in each field, NIRISS spectroscopy is taken with up to three filters (F115W, F150W, and F200W) and up to two orthogonal grism orientations (GR150R and GR150C). Direct imaging is also obtained for each field in up to three filters (F115W, F150W, and F200W). PASSAGE prioritizes maximizing spectroscopic coverage such that some fields have multigrism filter coverage but direct imaging in only one or two bands.

Exposure times for the survey fields vary from $\sim$1 to $\sim$20 hr, allowing for emission-line flux depths reaching between 10^{-17} and 10^{-18} cgs.

2.1. PASSAGE Fields in COSMOS

Fifteen out of the 63 PASSAGE fields lie within the COSMOS2020 HST/ACS footprint, as shown in the right panel of Figure 1. The left panels of Figure 1 show the typical emission-line flux sensitivity as a function of wavelength for each of these 15 fields (not all fields have all three filters), including both point and extended sources (emission lines from extended sources tend to have weaker significance than point sources). The color of each line encodes the integration time of the corresponding exposure, with darker shades indicating longer exposures. For the six fields that have observations in both orientations, the total exposure time is split approximately evenly between the two orientations.

These 15 fields and their observational properties are summarized in Table 1. Eight fields lie entirely within the COSMOS-Web footprint, three partially overlap COSMOS-Web (with the remaining area covered by the broader COSMOS2020 footprint), and four additional fields fall outside the COSMOS-Web footprint but remain within COSMOS2020.

Two fields have spectroscopy in all three filters (F115W, F150W, and F200W), eight fields were observed in two filters (F115W and F150W), and the remaining five were observed in a single filter, typically F200W (with the exception of Par051, which has only F115W coverage). Six fields include spectroscopy in at least one grism filter obtained at two orthogonal orientations using both GR150R and GR150C. Among these, Par028 stands out as one of the most complete PASSAGE fields, lying within the COSMOS-Web footprint and featuring the deepest observations in all three filters, each obtained at both orientations (see, e.g., A. Acharyya et al. 2025). In addition, several PASSAGE fields overlap with the JWST Cycle 3 COSMOS-3D survey (K. Kakiichi et al. 2024), which provides complementary NIRCam F444W WFSS data and imaging in F115W, F200W, and F356W.

2.2. Spectral Extraction

Slitless spectral extraction and contamination modeling are performed using the Grism Redshift and Line analysis software (GRIZLI; G. Brammer & J. Matharu 2021).[29] Redshift measurements are carried out separately as described below. A

[29] https://grizli.readthedocs.io, version 1.12.11.

Table 1
Observed PASSAGE Fields in Cosmos with Their Target Coordinates and Exposure Times

Field	Location	R.A. (deg)	Decl. (deg)	Obs. Date	F115W Direct (hr)	F150W Direct (hr)	F200W Direct (hr)	F115W Grism (hr)	F150W Grism (hr)	F200W Grism (hr)	SEP Obj.	CWT Obj.	Final Obj.
Par003	Cosmos-Web	150.4103959	2.4051779	2022-12-30	…	…	0.62	…	…	**1.24**[a]	3116	177	47
Par005	Cosmos2020	150.6536980	2.0855800	2023-01-07	0.43	0.43	…	**2.29**[a]	**2.29**[a]	…	4443	237	155
Par006	Cosmos2020	150.6762160	2.1293050	2023-01-06	0.43	0.43	…	**2.29**[a]	**2.29**[a]	…	4323	276	169
Par017	Cosmos-Web	150.3011088	1.8910817	2023-04-19	…	…	3.15	…	…	3.15	4526	612	68
Par020	Cosmos2020	149.6229230	2.2251060	2023-04-23	…	0.13	…	4.87	1.05	…	4186	283	176
Par023	Cosmos-Web	150.0655286	2.5519213	2023-05-01	…	0.13	…	4.29	1.05	…	4206	260	150
Par024	Cosmos-Web	150.1315237	2.4996595	2023-05-02	…	0.13	…	4.87	1.05	…	3890	208	119
Par025	Cosmos-Web	150.2457730	1.9774739	2023-05-02	…	0.13	…	4.87	1.05	…	3817	275	143
Par026	Cosmos-Web	150.1227170	2.4398773	2023-05-06	…	0.13	…	4.87	1.05	…	3744	231	152
Par028	Cosmos-Web	150.0874070	2.4185307	2023-05-20	1.79	1.43	1.43	**21.26**[a]	**7.08**[a]	**5.37**[a]	3614	894	285
Par029	Cosmos2020	150.2522870	1.7285570	2023-05-22	…	0.13	…	4.87	1.05	…	3708	218	123
Par049	Cosmos-Web (<50%)	149.7024380	2.0589470	2023-12-03	…	…	0.20	…	…	1.62	2826	251	117
Par051	Cosmos-Web (>50%)	150.5036633	2.2633940	2024-01-02	0.79	…	…	**7.09**[a]	…	…	3473	207	65
Par052	Cosmos-Web	150.1552214	2.0418390	2024-01-03	…	2.04	2.04	**12.02**[a]	3.94	3.94	4433	850	332
Par053	Cosmos-Web (>50%)	150.1030697	1.7931779	2024-01-04	…	…	0.20	…	…	1.62	2971	197	83

Notes. "Field" indicates the name of the parallel field within PASSAGE. The "Location" column indicates whether the field is fully in Cosmos-Web (denoted "Cosmos-Web"), fully in COSMOS2020 (denoted "COSMOS2020"), or partially in Cosmos-Web and partially in the larger COSMOS2020 footprint (>50% indicates most of the field is in Cosmos-Web, <50% indicates that less than half of the field is in Cosmos-Web). "R.A." and "Decl." indicate the central R.A./decl. pointing for each field. "Obs. Date" indicates the date of observations. "F115W/F150W/F200W direct" indicates the direct image exposure time for each field in each filter. "F115W/F150W/F200W grism" indicates the grism exposure time for each field in each filter. If a filter has no value, it indicates that there was no coverage in that filter. The bolded numbers indicate that there are both GRISMR and GRISMC observations for that filter. "SEP Obj." indicates the number of objects in each field that were identified in imaging by SEP. "CWT Obj." indicates the number of objects in each field that were identified as candidate emission-line sources by the CWT algorithm. "Final Obj." indicates the number of objects in each field that were confirmed as line emitters by the reviewers.

[a] Total exposure is split over both R and C grism orientations. The remaining fields only have one orientation.

detection image for each field is made by taking the weighted mean of all direct images for all filters that are available for that field. All sources in the detection image are identified using the Python Library for Source Extraction and Photometry (SEP; E. Bertin & S. Arnouts 1996; K. Barbary 2016).[30] SEP typically identifies between ∼3000 and 4500 sources in each field; these values are reported in Table 1. GRIZLI also measures photometric fluxes in each available filter from the direct images.

In order to model the overlapping spectra, GRIZLI takes the segmentation map of the SEP-identified sources and models their associated spectra in each individual grism exposure, providing both 2D and 1D spectra of each source for all available filters and orientations in each field. Combined 1D and 2D spectra are also generated for filters with multiple orientations.

Unfortunately, the spectral extraction performed by GRIZLI contains some noise and diffraction spikes that are incorrectly identified as extragalactic sources. Additionally, when GRIZLI processes the spectra of two overlapping traces, the automatic removal of the contamination is not perfect, occasionally resulting in an oversubtraction. These errors can result in the identification of fictitious extragalactic sources and spurious emission lines. Therefore, human intervention is essential to ensure an accurate sample of emission-line sources.

3. Emission-line Identification

Emission lines are identified in the GRIZLI-extracted spectra using a line-finding pipeline that performs automated detection of emission-line candidates, followed by visual inspection of all candidates. The code is made publicly available on GitHub (K. Nedkova et al. 2026),[31] and the automated and visual components of the pipeline are described in Sections 3.1 and 3.2, respectively. This pipeline has also been applied in other JWST WFSS surveys (A. J. Battisti et al. 2024; J. Kartaltepe et al. 2024).

3.1. Automated Line Detection

As part of this paper, we release the line-finding software used to identify emission lines and measure spectroscopic redshifts. Emission-line candidates in the reduced 1D spectra are identified using a continuous wavelet transform (CWT), which selects appropriately shaped peaks. This approach is described in detail in A. J. Battisti et al. (2024), where it was applied to HST/WFC3 WFSS data, and is based on the `find_peaks_cwt` routine from P. Du et al. (2006).

For completeness, we briefly summarize the algorithm here. Similar to a Fourier transform, the wavelet transform breaks the GRIZLI-extracted 1D signal into base constituents. However, rather than decomposing the signal into sinusoidal components like a Fourier transform, the base components are scaled and shifted versions of a "mother" Ricker wavelet, which is proportional to the second derivative of a Gaussian function. The CWT transform compares the wavelet with the PASSAGE 1D spectrum, shifting the wavelet along the spectrum's wavelength range and scaling (i.e., stretching/compressing) the wavelet. This process creates a matrix of CWT coefficients representing the correlation between the 1D spectrum and the wavelet across all wavelengths and scales. Emission-line candidates correlate with the wavelet over many scales and therefore appear as prominent "ridges" in the CWT coefficient matrix.

Thus, emission-line candidates are identified based on both amplitude and shape, reducing the number of spurious detections that require visual inspection.

The line-finding algorithm presented in A. J. Battisti et al. (2024) and M. Revalski et al. (2024) has been updated to enable reliable analysis of the PASSAGE data. In particular, the algorithm has been updated to handle up to three grism filters in as many as two orientations, which is crucial for analyzing NIRISS grism data. Additionally, the algorithm now automatically generates region files that can be applied to both direct and dispersed images, allowing inspectors to visually confirm the validity of identified emission lines and sources. The expected locations of bright zeroth orders are also marked in the dispersed images. This feature is critical as zeroth orders can be misidentified as emission features when they overlap with a trace. We note, however, that direct imaging is unavailable on one edge of the field (covering approximately 10% of the area), preventing the zeroth orders of some off-field objects from being marked. As described in A. J. Battisti et al. (2024), the original software fits emission lines with Gaussian functions and models the continuum by interpolating between user-defined nodes using a cubic spline. Both functions are retained in our updated version of the software, but we additionally allow emission lines to be fit with a double-Gaussian profile containing both narrow and broad components. Moreover, the continuum can now be fit using three functional families: splines, polynomials, and linear models. This added capability is necessary for the higher signal-to-noise ratio (SNR) JWST data (compared with the HST data on which the original software was based) and allows for more reliable line-flux and continuum measurements.

We require emission-line candidates to consist of at least three contiguous pixels and to have an emission-line SNR of $\mathrm{SNR_{line}} \geqslant 5$ (see also J. W. Colbert et al. 2013). This threshold corresponds to $\mathrm{SNR_{pixel}} \geqslant 2.88$. The number of emission lines identified by the automatic line-finding algorithm using a 5σ cutoff ranges from ∼250 to 1200 per field, depending on the exposure time and number of grism filters covered. This corresponds to ∼200–950 candidate emission-line sources per field (for a total of 5176 candidates), as some objects contain multiple emission lines. Given that only a minority of SEP-detected sources are expected to show emission lines within the covered spectral range, the line-finding algorithm typically excludes 75%–95% of sources per field from further consideration, efficiently reducing the candidate list for visual inspection. In general, more emission lines are identified in NIRISS filters at longer wavelengths. The increase in detected lines from F115W to F150W to F200W arises for three main reasons. First, the wavelength coverage of the grism increases from 0.27 μm in F115W to 0.34 μm in F150W and 0.47 μm in F200W. Second, the two typically strongest rest-frame optical emission lines, [O III] and Hα, are redshifted toward longer observed wavelengths, such that by $z \sim 1$ Hα falls outside the F115W bandpass, and by $z \sim 1.6$ [O III] does as well. Third, the number of artifacts that can masquerade as emission lines (such as zeroth-order images) increases from F115W to F200W. Unsurprisingly, the fields with coverage in all three

[30] https://sep.readthedocs.io
[31] https://github.com/jwstwfss/line-finding

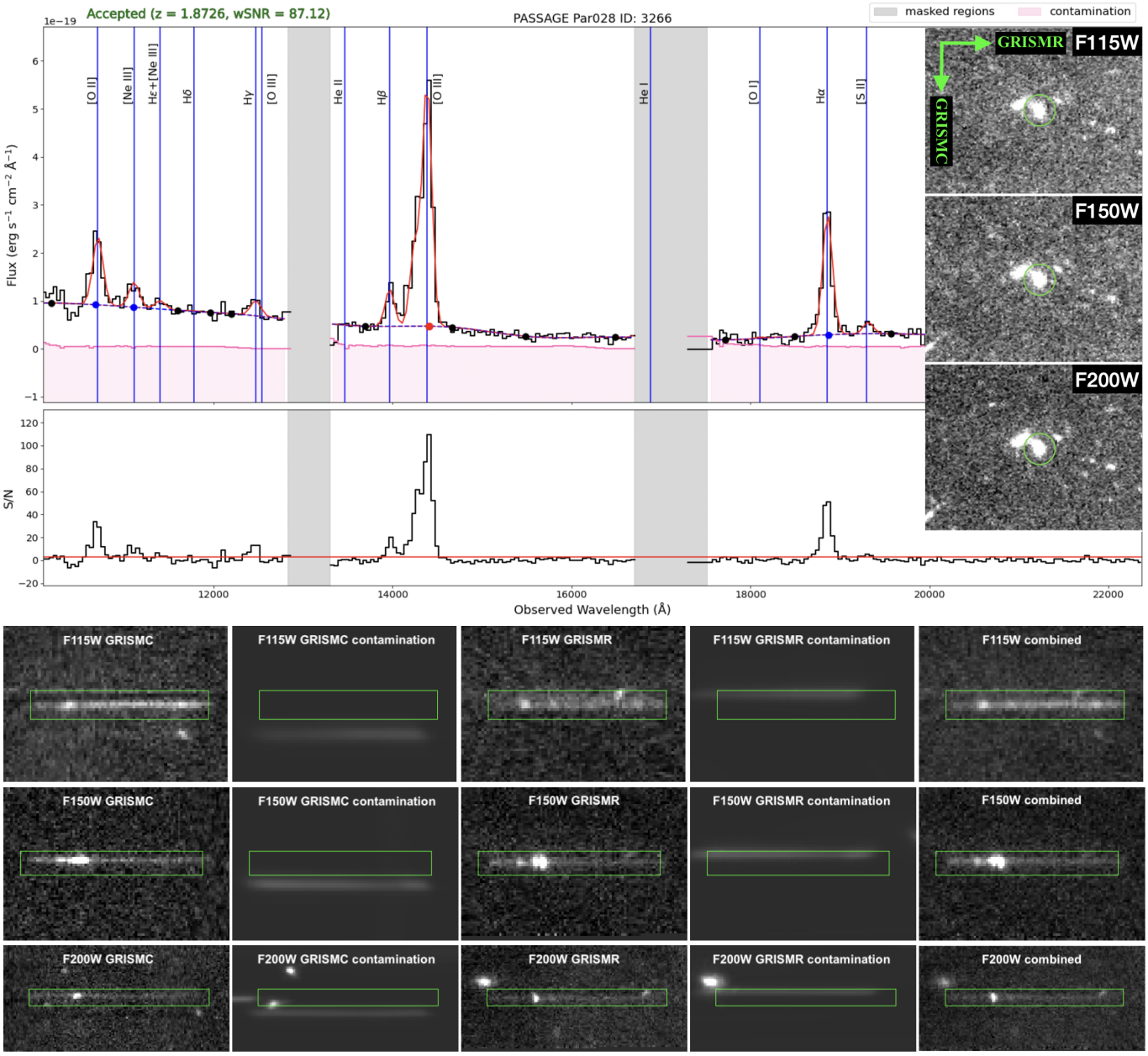

Figure 2. Visual interface of the emission-line-finding algorithm for an example galaxy at $z = 1.87$ in Par028, detected in all three filters in both grism orientations. The top panel shows the combined 1D spectrum of the galaxy (black), the contamination model (pink), and Gaussian fits to the emission lines (red). The observed wavelengths of the identified emission lines are marked with vertical blue lines. Gaps between the grism filters are shown in gray. The signal-to-noise ratio (S/N) of the spectrum at each wavelength is shown in the panel below the 1D spectrum. Cutouts of the direct images in F115W, F150W, and F200W are shown in the top right, with the target source circled in green. The green arrows represent the dispersion directions for the two GRISM orientations. The lower three rows show the 2D spectra for this object: the top row shows the F115W spectra, the middle row shows the F150W spectra, and the bottom row shows the F200W spectra. The first column shows the filters in the GRISMC orientation, the third column shows the GRISMR orientation, and the final column shows the orientation-combined 2D spectrum. The second and fourth columns show the GRISMC and GRISMR contamination models, respectively, marking spectral traces from neighboring sources and zeroth-order images. The GRISMR orientation contains several off-center emission lines originating from a neighboring source. This emphasizes the importance of obtaining observations in two orientations, as the GRISMC spectra confirm that these emission features belong to a different source.

grism filters (Par028 and Par052) yield the largest number of candidate emission lines.

Following the automated line-detection procedure, all emission lines are visually inspected to ensure their validity and confirm their redshifts.

3.2. Visual Line Confirmation

The line-finding algorithm enables visual inspection of every emission-line object identified by the CWT algorithm. Figure 2 shows the visual inspection interface for an example $z = 1.87$ source in Par028. The top panel shows the 1D spectrum in black, with the contamination model shown in pink. The grayed-out regions indicate masked spectral ranges (between the F115W and F150W filters on the left and F150W and F200W on the right). The locations of prominent emission lines are marked with vertical blue lines, and the corresponding features are modeled with Gaussian profiles shown in red. The continuum is traced by dashed blue lines, while the black points indicate the nodes used to constrain the

continuum as a spline. The SNR at each wavelength is shown in the panel below the 1D spectrum.

The direct images in the three filters are shown on the right, with the green circle indicating the target object. Gray-scale images of the 2D spectra are displayed in the lower three rows, corresponding to the NIRISS filters F115W, F150W, and F200W. The two grism orientations are shown in the first and third columns, with the orientation-combined spectrum shown in the final column. The contamination models in the second and fourth columns indicate possible contamination in each orientation. For this object, the strong emission lines are seen in both orientations and cannot be attributed to contamination from neighboring sources, indicating that the features are real. The high SNR of [O II], [O III], Hα, and Hβ indicates that this object has a highly robust redshift. The emission lines marked in the visual line-finder interface to assist with line identification and redshift determination can be found in Table 4 in Appendix A.

For every object in the field identified by the CWT algorithm, a (human) visual inspector examines the direct images, dispersed images, and both the 2D and 1D spectra. Only sources for which the automated line-detection algorithm identifies at least one emission-line candidate are advanced to visual inspection. Each of the 15 fields is independently reviewed by two inspectors. For each source, a spectroscopic redshift is assigned or the source is excluded from the final catalog if the object or its emission-line features are deemed spurious.

For a source to be assigned a spectroscopic redshift:

1. Reviewers must verify the reality of the source using the imaging data. Sources are removed from the catalog at this stage if they are determined to be noise fluctuations, detector artifacts, or saturated stars.
2. Reviewers must confirm that each emission feature is genuine. Emission-line candidates are rejected at this stage if they do not appear in both grism orientations when both GR150R and GR150C data are available, if the feature instead corresponds to a poorly fit continuum segment (often due to overlap with a neighboring spectral trace), if the signal originates from a zeroth-order image overlapping the spectrum (which is marked in the line-finder interface), or if it is caused by a diffraction spike from a nearby star crossing the spectral trace and mimicking an emission line in the 1D spectrum.
3. Reviewers must also verify that each emission line is correctly associated with the source and not with a different object, since misassociation can lead to double counting or incorrect redshift assignments. In particular, the spatial morphology of the emission feature should be consistent with that of the source, and the feature should be centered on the spectral trace. An example of an off-trace contaminant is shown in the F115W GRISMR 2D spectrum in Figure 2.

Object that fail any of these criteria are removed from the catalog. Sources that pass the visual inspection are assigned a spectroscopic redshift. These redshifts are primarily constrained using the following emission lines: Hα, [O III], [O II], Hβ, [S III], Paβ, and Paα. While additional emission features are denoted in the visual interface, the aforementioned emission lines are typically the strongest and most reliable for redshift determination.

For sources exhibiting multiple emission lines, the relative observed wavelengths must be consistent with the expected rest-frame line separations at a single spectroscopic redshift. The line-finding software allows users to assign a redshift, identify emission features as Hα, [O III], [O II], Hβ, [S III], Paβ, or Paα, or observed wavelengths at which individual lines are fit. A nonlinear least-squares optimizer based on the Levenberg–Marquardt algorithm is then used to fit the full spectrum, including the continuum. In practice, contamination from neighboring sources—particularly in fields observed in only a single grism orientation—and low-SNR emission lines can still lead to disagreements between reviewers, even for sources with multiple detected features. An additional complication arises for sources with spatially offset emission, which may result from clumpy star formation, mergers, accretion, and/or outflows. Such off-center emission can produce multiple peaks within a single spectral feature and is discussed further in Appendix B. For spectra containing a single emission line, the feature is assumed by default to be Hα, and the corresponding redshift is assigned. However, if the line profile exhibits sufficient asymmetry to indicate the presence of the [O III] doublet, the feature is instead identified as [O III], and the redshift is adjusted accordingly.

3.2.1. Reconciliation

After two reviewers have independently completed the visual inspection for each object in a field, there is a reconciliation procedure is conducted. During this step, the reviewers discuss all objects in the field for which there is disagreement either in the assigned redshift of the source or in the validity of the source (i.e., one reviewer removed the source from the catalog while the other assigned it a redshift). The reviewers must reach agreement on the redshift and legitimacy of the source to retain it in the final PASSAGE catalog. In the rare case that no agreement is reached, the source is assigned the lowest data-quality flag (see Section 3.2.2), and the line is assigned as Hα (or, for spectra with multiple emission lines, the strongest is assigned as Hα). This default assumption of Hα is based on the results from I. Baronchelli et al. (2020), who found that >50% of single-line emitters were correctly identified as Hα in the absence of ancillary photometry.

3.2.2. Redshift Quality Flags

The line-finding and reconciliation procedures include the assignment of data-quality flags to each source that reflect the varying confidence in the derived spectroscopic redshifts. For example, redshifts based on multiple emission lines are generally more robust than those derived from a single line. The criteria for each redshift scenario and the corresponding quality flags are summarized in Table 2. Lower flag values indicate higher-confidence spectroscopic redshifts. The most secure classification (flag = 1) is assigned to sources with multiple emission lines detected at SNR $\geqslant$ 5. Only a subset of emission lines—Hα, [O III], [O II], Hβ, [S III], Paβ, and Paα—are used in defining this and the lower-confidence flags (2–4), as these features provide the primary constraints on the redshift.

Table 2
Flags on PASSAGE Redshifts Scenarios and Hierarchy

Flag	Case	Number of Sources
1	Multiple emission lines with SNR $\geqslant 5$	858
2	One line with SNR $\geqslant 5$ and at least one other line with $2 \leqslant$ SNR < 5	425
3	Single [O III] blended doublet line (has signature asymmetry) with SNR $\geqslant 5$	110
4	Other single line with SNR $\geqslant 2$ or multiple lines with $2 \leqslant$ SNR < 5	379
1.5	Originally flag 4 single-line emitters that have been adjusted/confirmed photometrically	411

Note. A lower flag indicates greater confidence in the spectroscopic redshift. The flag of 1.5 is discussed in Section 5.1. The third column displays the number of sources corresponding with each redshift flag.

A flag of 2 corresponds to sources with a single emission line detected at SNR $\geqslant 5$ and at least one additional emission line with $2 \leqslant$ SNR < 5. Flags 1 and 2 therefore both denote multiline emitters. We note that although the automated CWT line-detection stage requires emission-line candidates to satisfy $\mathrm{SNR}_{\mathrm{line}} \geqslant 5$, lower-significance lines may still appear in the final catalog for two reasons: (1) multiline emitters often exhibit additional weaker lines at the expected wavelengths and relative strengths, which nonetheless provide robust redshift confirmation, and (2) during visual inspection, reviewers may adjust the continuum fit to improve the overall spectral modeling, which can in some cases reduce the measured line SNR.

A flag of 3 is assigned to sources for which reviewers identify a single [O III] emission line with SNR $\geqslant 5$. The characteristic asymmetry of the [O III] doublet, which has an intrinsic flux ratio of ∼1:3 (P. J. Storey & C. J. Zeippen 2000), distinguishes it from other single-line features, resulting in a more reliable redshift than for other single-line emitters.

A flag of 4 is assigned to all remaining single-emission-line sources with SNR $\geqslant 2$, as well as to sources with multiple emission lines for which all features have $2 \leqslant$ SNR < 5. For single-line flag 4 sources, the spectroscopic data alone provide limited redshift discrimination without photometric information; accordingly, approximately 80% of these sources are provisionally identified as Hα emitters during the line-finding process. A small number of weak multiline sources also fall into this category, and their redshift assignments are likewise uncertain.

In Section 5.1, we incorporate COSMOS photometric constraints for sources located within the overlap between PASSAGE and COSMOS, which in some cases refine or confirm the redshifts of flag 4 sources in hindsight. However, the line-finding procedure is intentionally performed without prior redshift information in order to assess the intrinsic reliability of the PASSAGE spectroscopic redshift assignments and to prepare for analyses of PASSAGE fields lacking ancillary photometric data.

We note that additional emission lines (e.g., [Ne III], Paγ, [S II], [O I], He I, Mg II, and higher-order Balmer lines such as Hγ and Hδ) may be present in some spectra but are typically too weak to be used reliably in the redshift-flagging scheme. In cases where such lines are detected at high significance, the redshift is already robustly constrained by one or more of Hα, [O III], [O II], Hβ, [S III], and/or Paβ.

A notable exception to the standard flag hierarchy is a highly secure $z = 4.64$ quasar in Par028, which exhibits strong [O II], [Ne III], Mg II, and C III] emission. Although this source would nominally be assigned flag 4 under the standard criteria, it is upgraded to flag 1 in the final catalog due to the unambiguous nature of its spectral features.

4. Results

4.1. Statistics of Rejected Sources

The CWT automated line-detection algorithm initially identified 5175 emission-line candidates within the COSMOS-Web/COSMOS2020 footprint. Following visual inspection (Section 3.2), 2183 sources were retained with assigned spectroscopic redshifts in the final PASSAGE catalog, while 2992 candidates were rejected. Emission-line candidates were removed either because the source itself was determined to be spurious or because the identified emission line(s) were not deemed to be genuine.

On average, 53% of the emission-line candidates identified by the CWT algorithm were rejected during visual inspection, with a majority of candidates rejected in seven of the 15 fields. This underscores the critical role of visual inspection: While the CWT algorithm substantially reduces the number of sources requiring review, it necessarily identifies a significant number of false-positive emission-line candidates. Common contaminants, such as stellar diffraction spikes, zeroth-order images, and overlapping spectral traces, can be readily recognized by human reviewers but remain challenging to identify reliably using automated methods alone.

Although a rejection rate of ∼53% may appear high, it is significantly lower than in comparable studies that rely on direct visual inspection of all GRIZLI-extracted sources. For example, G. Noirot et al. (2023) identified 156 line emitters from 1394 sources, and P. J. Watson et al. (2025a) identified 488 line emitters from 3694 sources, corresponding to rejection rates exceeding 85% in both cases. The use of the CWT algorithm therefore acts as an effective prefilter, increasing the success rate of visual inspection to ∼50%, depending on the field.

Raising the CWT detection threshold from 5σ to 10σ would further reduce the number of candidates requiring visual inspection, eliminating roughly 40% of the sources identified at the 5σ level. However, this change would also result in the loss of approximately 30% of the sources ultimately accepted by the reviewers, substantially reducing the size of the final emission-line sample. For reference, reviewers reject approximately 65% of candidates with at least one emission line detected at SNR > 5, compared to ∼55% of candidates with at least one line at SNR > 10. These trends further demonstrate that visual inspection remains essential for mitigating contamination and constructing a reliable spectroscopic sample.

Table 3
Format of the Redshift Catalog

Label	Description	Example Value
ID	Source identifier	1428
RA	R.A. (deg)	150.085539
DEC	Decl. (deg)	2.43329
FIELD	PASSAGE field the object lies in	Par028
Z_BEST	Best PASSAGE spectroscopic redshift	1.8735
EMLINE_FLAG	Flag on the PASSAGE spectroscopic redshift	1
Z_BEST_ERR	Best redshift error	0.0000
Z_PASSAGE_LINEFINDER	Spectroscopic redshift determined through PASSAGE line-finding	1.8735
Z_PASSAGE_ERR	Error on the PASSAGE spectroscopic redshift	0.0000
COSMOSWEB_ID	Source identifier in COSMOS2025/COSMOS-Web	423415
COSMOS2020_ID	Source identifier in CLASSIC COSMOS2020 catalog	1070736
CONFUSION_FLAG	Confusion flag if multiple COSMOS objects could be matched with a single PASSAGE object	0
AGN_FLAG	Flag if COSMOS-Web indicates the source is likely an AGN	0
WARN_FLAG	COSMOS-Web warning flag	0
MASS_50	Stellar mass of the source (50th percentile), $\log_{10}(M_*/M_\odot)$	8.601055
MASS_84	84th percentile on stellar mass, $\log_{10}(M_*/M_\odot)$	8.664838
MASS_16	16th percentile on stellar mass, $\log_{10}(M_*/M_\odot)$	8.532257
F115W_NIRISS_FLUX	PASSAGE F115W auto flux (μJy)	0.394123
F115W_NIRISS_ERR	PASSAGE F115W auto flux error (μJy)	0.005081
F150W_NIRISS_FLUX	PASSAGE F150W auto flux (μJy)	0.589730
F150W_NIRISS_ERR	PASSAGE F150W auto flux error (μJy)	0.005962
F200W_NIRISS_FLUX	PASSAGE F200W auto flux (μJy)	0.485601
F200W_NIRISS_ERR	PASSAGE F200W auto flux error (μJy)	0.005316

Note. PASSAGE sources with no corresponding photometric match are given a −99 for any column requiring COSMOS data. The R.A. and decl. are given in epoch J2000.

(This table is available in its entirety in machine-readable form in the online article.)

4.2. Spectroscopic Redshift Catalog

We present the PASSAGE spectroscopic redshift catalog in the COSMOS field, which can be found in the online journal (see Table 3) and on GitHub.[32] In total, the line-finding effort identifies 2183 emission-line sources, corresponding to 3208 emission lines detected at SNR > 5, as many sources exhibit multiple lines.[33]

Each PASSAGE emission-line source is crossmatched with the COSMOS-Web and COSMOS2020 (CLASSIC) catalogs. A match is assigned to the nearest COSMOS source within a 0.″3 radius, chosen to correspond to the NIRCam F444W point-spread function FWHM, which is relevant for stellar-mass measurements (Section 7). If multiple COSMOS sources fall within this radius, the object is flagged as potentially confused (CONFUSION_FLAG) in the catalog. For crossmatched sources, the PASSAGE spectroscopic measurements are supplemented with multiband COSMOS photometric data.

Of the 2183 emission-line sources, 1332 are matched to COSMOS-Web objects, 564 are matched to COSMOS2020 sources outside the COSMOS-Web footprint, and 287 have no counterpart in either COSMOS catalog. Based on the spectroscopic quality flags defined in Section 3.2.2, 858 sources are assigned flag 1, 425 flag 2, 110 flag 3, and 790 flag 4; thus, the largest fraction of the catalog consists of the highest-confidence (flag 1) redshifts.

The catalog format is summarized in Table 3. It includes spectroscopic redshifts, quality flags, photometric fluxes, and stellar masses (Section 7) for all PASSAGE emission-line sources detected in the 15 fields listed in Table 1. The measured emission-line fluxes and uncertainties will be presented in a forthcoming paper (K. V. Nedkova et al. 2026, in preparation). The preferred redshift and its associated uncertainty are provided in Z_BEST and Z_BEST_ERR. COSMOS-Web and COSMOS2020 source identifiers are included for all crossmatched objects, while sources without COSMOS counterparts are retained in the catalog and assigned placeholder values of −99 for parameters requiring COSMOS photometric data.

Several quality and classification flags are included. The EMLINE_FLAG encodes the PASSAGE spectroscopic redshift confidence described in Section 3.2.2. The WARN_FLAG mirrors the COSMOS-Web quality flag (indicating that a COSMOS-Web source may be a hot pixel, or that ground- and space-based photometry are inconsistent with one another). The AGN_FLAG identifies sources classified as likely AGN in COSMOS-Web, as their photometry is better fit with an AGN SED template than a galaxy template. This flag indicates that the derived stellar masses in Section 7 may be unreliable.

The column Z_PASSAGE_LINEFINDER records the redshift assigned during the line-finding procedure (with uncertainty Z_PASSAGE_ERR) and matches Z_BEST for the vast majority of sources. For a subset of single-line emitters, the redshift is refined in Section 5.1 using COSMOS photometric information.

5. Redshift Comparison

The overlap between PASSAGE and COSMOS provides both spectroscopic and photometric redshift measurements for

[32] https://github.com/huber458/Passage-in-Cosmos-Linelist-Catalog

[33] Due to the slight overlap between Par026 and Par028, one emission-line source appears in both fields. The redshift measured for this object is consistent across both fields; however, it is assigned a flag of 1 in Par028, where both Hα and [S III] are detected, and a flag of 4 in Par026, where only Hα is detected because of more limited wavelength coverage. To avoid double counting, we retain the Par028 measurements for this source.

a large sample of sources. We begin by comparing the redshifts derived from these two catalogs.

5.1. Photometric Redshift Comparison

The availability of both PASSAGE and COSMOS data enables consistency checks between independent redshift measurements. COSMOS-Web photometric redshifts have been shown to be fairly accurate. Simulations conducted in C. M. Casey et al. (2023) found that the normalized median absolute deviation, $\sigma_{\rm NMAD}$ (a measure of variation that suppresses outliers), defined as

$$\sigma_{\rm NMAD} = 1.48 \times \text{median}\left(\left|\frac{\Delta z}{1+z} - \text{median}\left(\frac{\Delta z}{1+z}\right)\right|\right) \quad (1)$$

following D. C. Hoaglin et al. (1983), G. B. Brammer et al. (2008), C. M. Casey et al. (2023), B. Wang et al. (2024), and J. Ratajczak et al. (2026), where

$$\frac{\Delta z}{1+z} = \frac{z_{\rm phot} - z_{\rm spec}}{1+z_{\rm spec}} \quad (2)$$

between photometric redshifts fit to mock galaxies using the full suite of COSMOS-Web filters and the true spectroscopic redshifts is $\sigma_{\rm NMAD} = 0.033$. This demonstrates the generally high accuracy of COSMOS-Web photometric redshifts. However, without spectroscopic information, these photometric redshifts are often accompanied by large uncertainties and can include sources with catastrophic redshift errors (e.g., C. M. Casey et al. 2023; J. Ratajczak et al. 2026). In contrast, the PASSAGE spectroscopic redshifts have very low uncertainties (typically on the order of 0.0005), assuming that all emission lines in PASSAGE spectra have been identified correctly. Realistically, not all emission lines in PASSAGE will have been identified correctly (see I. Baronchelli et al. 2020, 2021; K. Boyett et al. 2024), and thus this assumption is only true for a subset of galaxies. The key question is therefore: For which subset of sources are the PASSAGE redshifts reliable? For PASSAGE flag 1 multiline emitters, the identities of the emission lines are extremely reliable, since it is difficult to reproduce the observed distribution of strong emission lines, especially their relative fluxes, with an incorrect line identification. By contrast, the PASSAGE redshifts for flag 4 single-line emitters can still precisely constrain the peak of the single emission line, but the lack of additional lines within the wavelength range often makes the identity of the single emission line ambiguous. In these instances, the COSMOS photometry can frequently help distinguish the true identity of the single-line emitter.

In the top panel of Figure 3, we compare COSMOS-Web crossmatched PASSAGE spectroscopic redshifts with COSMOS-Web photometric redshifts. In the bottom panel, we repeat this comparison, but for COSMOS2020 crossmatched sources located outside the COSMOS-Web footprint. Point color indicates the spectroscopic quality flag, while the marker size scales with ACS/F814W magnitude, with smaller markers indicating fainter magnitudes. The solid black line represents the 1:1 line. For the combined COSMOS-Web/COSMOS2020 sample, 65% of redshifts agree within $|\Delta z| = |z_{\rm phot} - z_{\rm spec}| \leqslant 0.2$, and 78% of redshifts agree within $|\Delta z| \leqslant 0.5$. This indicates that, in the vast majority of cases, $z_{\rm PASSAGE}$ and $z_{\rm COSMOS}$ are in relatively good agreement. This level of agreement depends on the redshift flag: For the subset of sources with a quality flag of 1, we find $\sigma_{\rm NMAD} = 0.036$, indicating very strong agreement between the photometric and spectroscopic redshifts. This essentially mirrors the level of agreement found in the aforementioned simulations of C. M. Casey et al. (2023), which compared photometric and spectroscopic redshifts in COSMOS-Web. That said, for the flags 2 and 3 subsets, $\sigma_{\rm NMAD}$ increases to $\sigma_{\rm NMAD} = 0.071$ and $\sigma_{\rm NMAD} = 0.109$, respectively, indicating an increasingly weaker redshift agreement. For the flag 4 subset, $\sigma_{\rm NMAD} = 0.094$, indicating a relatively weak redshift agreement. However, the flag 4 distribution shows an overabundance of sources lying near the dashed and dotted black lines in Figure 3. The dashed line corresponds to cases where PASSAGE reviewers classify a single emission line as Hα (our conservative default choice), whereas the COSMOS photometry instead favors [O III]. Likewise, the dotted line corresponds to cases where the PASSAGE reviewers classify a single emission line as Hα, but the COSMOS photometry instead favors [O II]. Therefore, with the benefit of hindsight, it is likely that many of the sources lying close to these lines are misidentified ambiguous single-line emitters.

For a subset of flag 4 single-line sources initially identified as Hα emitters, we refine the PASSAGE spectroscopic redshifts using COSMOS photometric redshift information. This refinement assumes that, in some cases, the single detected emission line was misidentified as Hα and instead corresponds to [O III] (dashed-line scenario) or [O II] (dotted-line scenario). Because the observed wavelength of the emission feature is well constrained by PASSAGE, directly adopting the COSMOS photometric redshift is not appropriate. Instead, we compute an adjusted redshift using

$$z_{\rm best} = \frac{\lambda_{\rm H\alpha,0}}{\lambda_{\rm OIII,0}}(1+z_{\rm spec}) - 1 \quad (3)$$

for the [O III] case, and

$$z_{\rm best} = \frac{\lambda_{\rm H\alpha,0}}{\lambda_{\rm OII,0}}(1+z_{\rm spec}) - 1 \quad (4)$$

for the [O II] case.

This refinement is applied to all single-line Hα-designated sources that lie within $5\sigma_{\rm NMAD}$ of the dashed or dotted loci in Figure 3, where $\sigma_{\rm NMAD} = 0.037$ is derived from the robust flag 1 sample. This threshold corresponds approximately to sources within $\Delta z \simeq 0.18$ of the expected loci.

Sources whose redshifts are refined in this manner are assigned the refined redshift in the ZBEST column of the catalog, while the original redshift from the line-finding effort is retained in the Z_PASSAGE_LINEFINDER column. These sources are also reclassified as flag 1.5, together with flag 4 sources that already show strong agreement between $z_{\rm PASSAGE}$ and $z_{\rm COSMOS}$ within the same $5\sigma_{\rm NMAD}$ threshold. This designation reflects that these redshifts are substantially more reliable than those of the remaining flag 4 sources. After this procedure, 183 flag 4 sources with COSMOS counterparts remain discrepant, with $\sigma_{\rm NMAD} = 0.400$, and an additional 224 flag 4 sources lack COSMOS counterparts entirely. The PASSAGE spectroscopic redshifts for these 407 sources should therefore be treated with caution. In contrast, 383

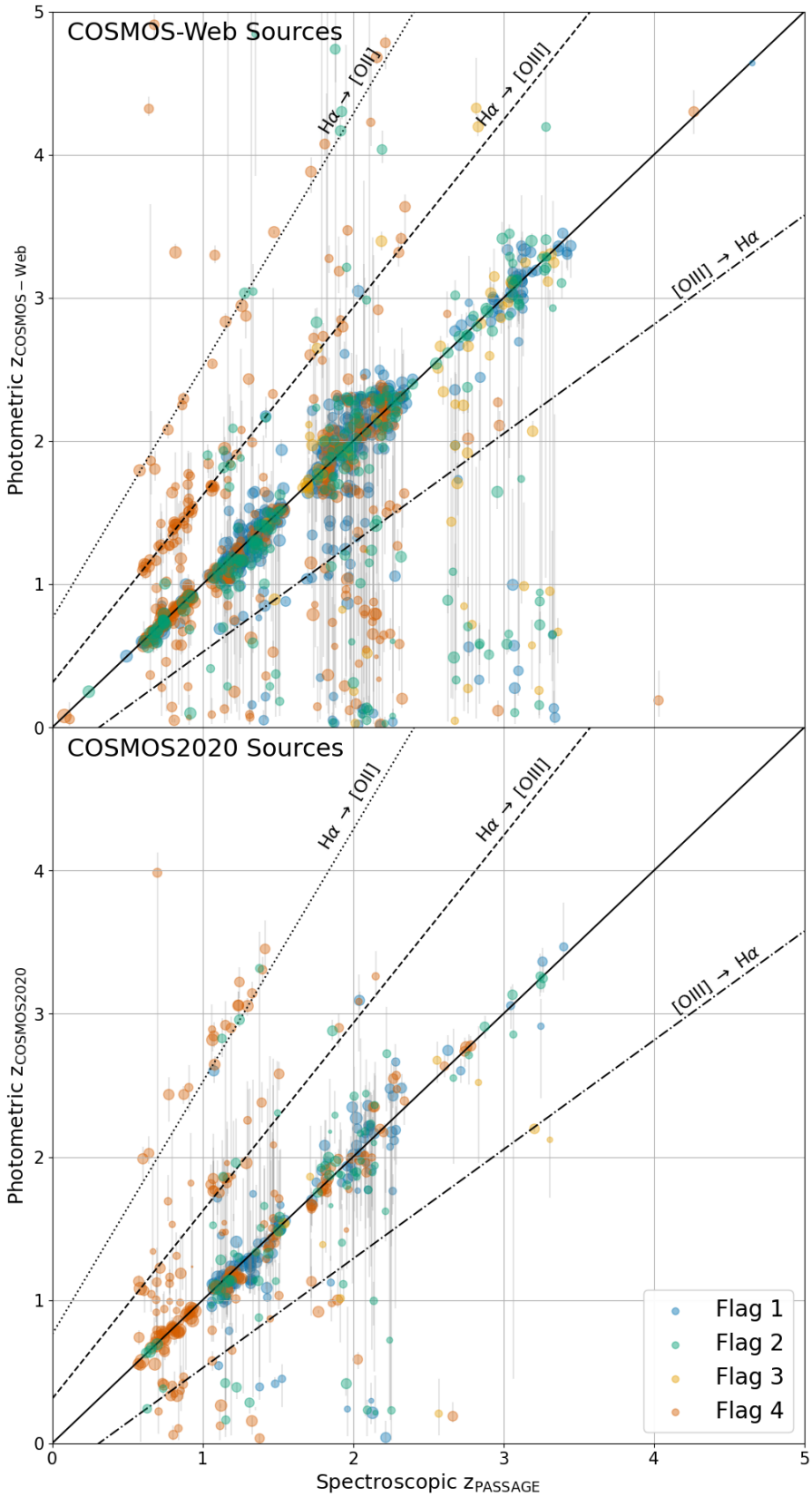

Figure 3. Comparison of photometric redshifts from COSMOS-Web (top panel) and COSMOS2020 (bottom panel) with spectroscopic redshifts from the PASSAGE line-finding analysis. Point color indicates the spectroscopic quality flag, while marker size scales with ACS/F814W magnitude, with smaller markers indicating fainter magnitudes. The solid line represents an exact 1:1 match in redshift. The dashed (dotted) line traces the redshifts where the PASSAGE team identifies a line as Hα, but the corresponding redshift from COSMOS-Web instead favors [O III] ([O II]). The dashed–dotted line traces the redshifts where the PASSAGE team identifies a line as [O III], while COSMOS-Web photometry instead favors Hα.

sources are classified as flag 1.5, exhibiting $\sigma_{\rm NMAD} = 0.022$, and their redshifts can be considered robust.

Although photometric redshifts are themselves subject to uncertainties, the accuracy demonstrated in simulations by C. M. Casey et al. (2023), combined with the fact that nearly all sources with $z_{\rm COSMOS} > z_{\rm PASSAGE}$ lie close to the expected [O III] and [O II] loci, suggests that this adjustment provides the most plausible redshift estimates for the majority of flag 1.5 sources. In total, 81 [O III] lines and 27 [O II] lines are reidentified through this process, corresponding to approximately 14% and 5%, respectively, of all crossmatched flag 4 sources. Thus, with the benefit of photometric hindsight, we estimate that ∼19% of flag 4 single-line sources were initially misidentified.

The number of photometrically adjusted redshifts varies by field configuration. The five single-filter fields account for 33 adjusted sources, the eight two-filter fields for 65, and the two three-filter fields for 10. This distribution is expected, as fields with more limited wavelength coverage naturally produce a larger fraction of flag 4 sources. Notably, Par051 alone contributes 20 adjusted redshifts, nearly one-fifth of the total. Unlike the other single-filter fields, which were observed in F200W, Par051 was observed only in F115W, where the lower spectral resolution makes the characteristic asymmetry of the [O III] doublet more difficult to identify during visual inspection. As a result, sources that would otherwise be classified as flag 3 are more likely to be classified as flag 4 in this field, consistent with Par051 also having the fewest flag 3 sources of any field.

One consequence of this photometric refinement is that many of the highest-redshift sources in the catalog ($3 < z < 5$) are identified through this adjustment, primarily as single [O II] emitters detected in F200W, which are otherwise difficult to distinguish from Hα without photometric context. This has important implications for the remaining PASSAGE fields outside COSMOS, as well as for PASSAGE sources without COSMOS counterparts: In the absence of ancillary photometric data, flag 4 single-line sources are likely to be misidentified at the ∼19% level.

An additional overdensity is visible in Figure 3 along the dashed–dotted line. This locus corresponds to cases where COSMOS photometric redshifts favor interpreting a PASSAGE-identified [O III] emission feature as Hα. However, the majority of sources near this locus are multiline emitters rather than flag 3 single-line sources, and reexamination of the spectra confirms the robustness of the PASSAGE redshift assignments.

A likely contributor to this overdensity is the absence of F200W imaging in COSMOS-Web. While JWST/NIRCam provides imaging in F115W, F150W, F277W, and F444W, it does not include F200W coverage. A common configuration for sources in this region of parameter space is the presence of [O III] emission in F150W and Hα emission in F200W. Although PASSAGE spectroscopic redshifts for these sources are well constrained, the lack of F200W imaging in COSMOS can lead SED-fitting codes to misinterpret the strong F150W flux as originating from Hα rather than [O III].

Several factors contribute to discrepancies between robust PASSAGE spectroscopic redshifts and COSMOS-Web redshifts. Many COSMOS-Web sources have large uncertainties, so that even discrepant best-fit values remain consistent within 1σ. Some sources have a poor fit to the photometry, as indicated by a high χ^2 value in the M. Shuntov et al. (2025) catalog. Some sources have multiple peaks in the $P(z)$ that are not well reflected by the error bars, indicating that several redshift ranges can fit the observed photometry. Other sources are among the faintest objects in the sample, for which redshift disagreements are not unexpected.

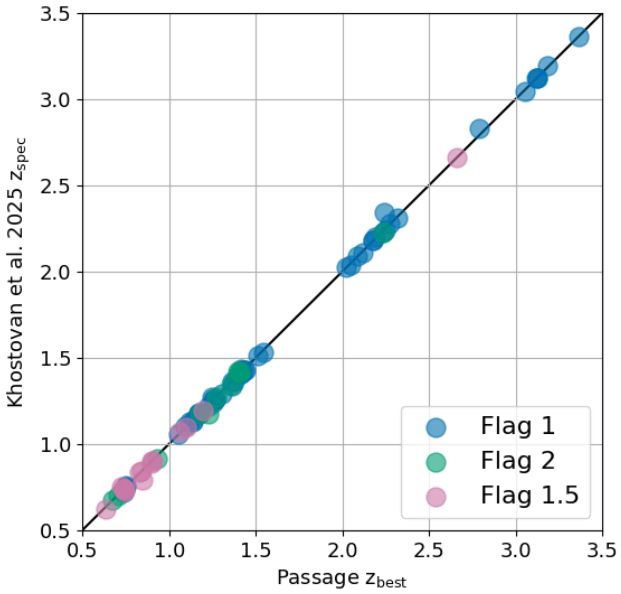

Figure 4. Spectroscopic redshift comparison between the PASSAGE redshifts and the ancillary spectroscopic redshifts compiled in A. A. Khostovan et al. (2026). Only high-quality spectroscopic redshifts from A. A. Khostovan et al. (2026; $Q_f = 3, 4$) and PASSAGE (flags 1, 2, and 1.5) are included in the comparison.

5.2. Spectroscopic Redshift Comparison

We now compare the PASSAGE spectroscopic redshifts to previously obtained spectroscopic redshifts. A. A. Khostovan et al. (2026) recently presented a compilation of COSMOS spectroscopic redshifts encompassing ∼20 yr of spectroscopic redshifts over a ∼10 deg^2 area centered on the COSMOS legacy field. Using the same crossmatching parameters as in Section 4.2, we crossmatch the PASSAGE catalog with the A. A. Khostovan et al. (2026) compilation. In total, there are 228 crossmatched sources between the two catalogs. We restrict our comparison to the 81 of these 228 sources that have robust redshift measurements in both samples (i.e., sources with a quality flag of $Q_f = 3$ or 4 in A. A. Khostovan et al. 2026 and a flag of 1, 2, or 1.5 in PASSAGE). In the A. A. Khostovan et al. (2026) sample, a source with $Q_f = 3$ or 4 corresponds to >95% confidence in the reported redshift (see Appendix C for a comparison including lower-quality flags). In Figure 4, we show the comparison between the A. A. Khostovan et al. (2026) spectroscopic redshifts and the PASSAGE spectroscopic redshifts. All 81 crossmatched sources agree between the two catalogs at the level of $|z_{\rm Khostovan+} - z_{\rm best}| < 0.1$.

This comparison also emphasizes the value of PASSAGE (and NIRISS more generally) in providing a legacy dataset of spectroscopic redshifts. The 15 ∼2.′2 × 2.′2 PASSAGE fields provide 2183 spectroscopic redshifts, of which only 228 sources had previously published spectroscopic redshifts (of varying quality). This means that PASSAGE has delivered 1955 new spectroscopic redshifts in COSMOS for sources that

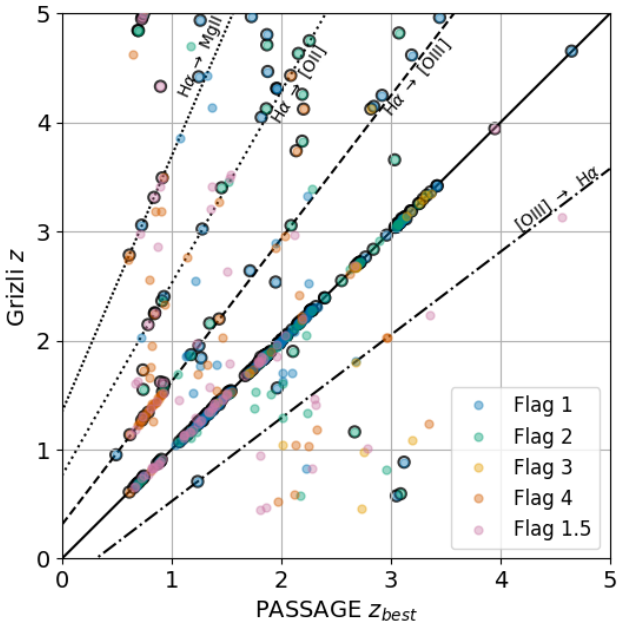

Figure 5. Spectroscopic redshift comparison between the $z_{\rm best}$ PASSAGE redshifts and the GRIZLI-derived spectroscopic redshifts for four PASSAGE fields. Sources from Par028 are circled with a black outline.

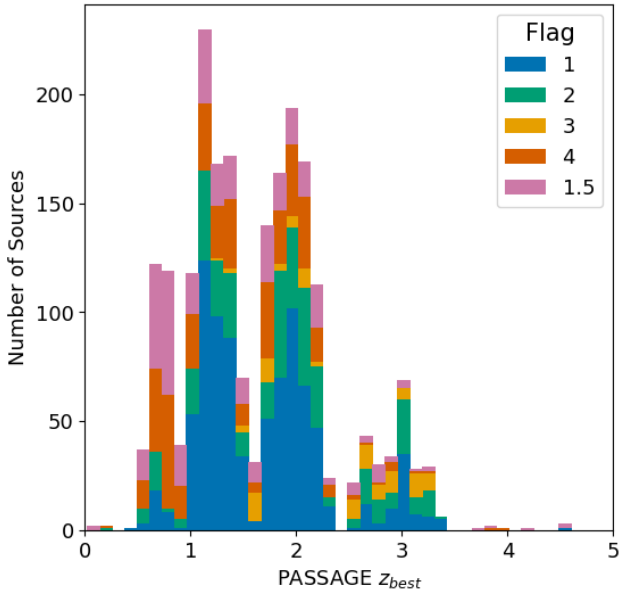

Figure 6. Histogram of the final PASSAGE spectroscopic redshifts, $z_{\rm best}$. The stacked histogram is subdivided by redshift quality flag. We identify sources spanning a redshift range of $0.08 \lesssim z_{\rm spec} \lesssim 4.7$.

previously lacked such measurements, demonstrating the strength of the pure-parallel approach with NIRISS.

5.3. Redshift Comparison to GRIZLI

It is also informative to compare the redshifts obtained from the line-finding procedure with those derived from blindly running the GRIZLI algorithm. For Par003 (F200W only), Par025 (F115W and F150W), Par028 (F115W, F150W, and F200W), and Par051 (F115W only), representing each combination of NIRISS filters used in this study, we compare the GRIZLI-predicted redshifts to $z_{\rm best}$. This comparison is shown in Figure 5, and excludes sources rejected by reviewers (for which GRIZLI would have blindly assigned a redshift).

Just 65% of the sources in this sample show a redshift agreement of $|z_{\rm Grizli} - z_{\rm best}| < 0.1$. Flag 1 sources tend to agree in redshift (85% of flag 1 sources have $|z_{\rm Grizli} - z_{\rm best}| < 0.1$), but this discrepancy decreases for lower-quality flags (down to 52% for flag 2 sources). However, even in the flag 1 subset, there are noticeable outliers. For example, a flag 1 object in Par028 has $z_{\rm best} = 1.82$ and $z_{\rm Grizli} = 4.04$. The $z_{\rm best} = 1.82$ redshift assignment comes from Hα, [O III], and Hβ emission lines observed in both grism orientations. However, the $z_{\rm Grizli} = 4.04$ would assign Mg II to only the [O III] peak and does not account for the legitimate Hα peak. A number of single-line emitters are similarly assigned Mg II by GRIZLI (see sources near the densely dotted line in Figure 5), whereas the line-finding procedure (and in some cases the COSMOS photometry) prefers an Hα determination.

For the flag 1.5 sources where the line-finding $z_{\rm spec}$ agrees with $z_{\rm COSMOS}$ (ignoring for the moment the subset of flag 1.5 sources with photometrically "adjusted" redshifts), only 33% of GRIZLI redshifts agree within $\Delta z \leqslant 0.1$ with the other two measurements of redshift (which are in agreement with each other). This means that, for this selection of single-line emitters, GRIZLI is actually more likely to disagree than agree with $z_{\rm best}$.

Restricting the comparison to Par028 alone (the three-filter field, indicated by points with black circles in Figure 5), 75% of redshifts agree between the GRIZLI z and $z_{\rm best}$. For Par028 flag 1 sources only, this agreement rises to 88%. This suggests that the primary disagreement between the two approaches arises from sources with only one emission line within the wavelength coverage. For flag 1 multiline emitters, discrepancies can arise from the similar spacing between different pairs of strong emission lines (e.g., the similarity between the wavelength separations of Hα and Hβ and [O III] and [O II]).

We also compare these GRIZLI redshifts directly with COSMOS-Web photometric redshifts. The resulting $\sigma_{\rm NMAD} = 0.082$ is larger than the corresponding comparison between the line-finding redshifts (prior to any photometric redshift adjustments) and the COSMOS-Web redshifts, which yields $\sigma_{\rm NMAD} = 0.062$. This comparison to GRIZLI does not include any of the sources rejected by reviewers during visual inspection, meaning that GRIZLI would still assign redshifts to objects deemed spurious in our analysis. This does not imply that GRIZLI is incorrect in cases of disagreement with both COSMOS-Web and the line-finding procedure, but it is a strong indicator that GRIZLI is typically less accurate than the line-finding and visual inspection procedure. Therefore, the line-finding and visual inspection procedure is essential for obtaining the most accurate spectroscopic redshifts.

6. Redshift Statistics

We now proceed with the full catalog, including the newly defined flag 1.5 sources, and examine its statistical properties, beginning with the redshift distribution. Figure 6 shows a stacked histogram of spectroscopic redshifts in the COSMOS PASSAGE catalog, with each bin subdivided by redshift quality flag. The three prominent gaps in the redshift distribution at $z \sim 1$, $z \sim 1.6$, and $z \sim 2.4$ correspond to redshift ranges where Hα, [O III], and [O II] fall into the $\sim$13000 Å and $\sim$17000 Å gaps between the F115W/F150W

and F150W/F200W filter bandpasses, respectively (see Figure 2).

Galaxies with high-confidence flags (1 and 2) lie primarily in the $1.0 \lesssim z_{\rm spec} \lesssim 3.4$ range. This is because, in multifilter fields, Hα and [O III] can be observed in neighboring NIRISS filters over $1.0 \lesssim z_{\rm spec} \lesssim 2.3$, while [O III] and [O II] can appear in neighboring NIRISS filters together over $1.7 \lesssim z_{\rm spec} \lesssim 3.4$. Flag 3 sources become more prevalent at higher redshifts. This flag is most commonly assigned in single-filter fields, where, as discussed in Section 5.1, the characteristic asymmetry of the [O III] doublet is more readily identified in the F200W grism. [O III] can be detected in F200W over the redshift range $2.4 \lesssim z_{\rm spec} \lesssim 3.4$. At $z \gtrsim 3.5$, redshifts are most often assigned when [O II] falls within the F200W bandpass. In many cases, this identification is only possible through the photometric redshift refinement, unless additional features such as [Ne III] or higher-order Balmer lines are also detected. A small number of sources at these redshifts exhibit Mg II emission, potentially indicating the presence of an AGN.

At the low-z end, line identification is dominated by [S III] and Paβ lines. For a source to have $z \lesssim 0.5$, [S III] must be detected in either F115W or F150W, and/or Paβ must be identified in F150W or F200W. Single-line Hα emitters are typically classified as flag 4 or flag 1.5 sources at $0.5 \lesssim z \lesssim 1$ in F115W, at $1 \lesssim z \lesssim 1.7$ in F150W and at $1.7 \lesssim z \lesssim 2.2$ in F200W. The redshift range $1.7 \lesssim z \lesssim 2.2$ contains some of the most robust redshift measurements, as in three-filter fields Hα, [O III], Hβ, and [O II] all fall within the NIRISS wavelength coverage. This makes this interval particularly well suited for metallicity studies and dust corrections using the Balmer decrement.

7. Stellar Masses

The stellar masses of emission-line sources crossmatched between PASSAGE and COSMOS are derived using COSMOS-Web photometry, with updated redshifts and additional PASSAGE photometry in the NIRISS F115W, F150W, and F200W filters where available. Owing to differences in data reduction and photometric extraction methods, we use here only photometry from the COSMOS-Web Data Release 1 (DR1) release (M. Shuntov et al. 2025), rather than combining it with COSMOS2020 data. We use `SourceXtractor++` (hereafter SE++; E. Bertin et al. 2020; M. Kümmel et al. 2022) fluxes in all available bands, together with PASSAGE NIRISS `auto` fluxes (see Table 3). In cases where multiple PASSAGE sources match a single COSMOS-Web source, due to the deblending parameters chosen in Section 2.2, we rescale the COSMOS-Web fluxes for each source by the ratio of their PASSAGE `flux_auto` measurements.

As the NIRISS filters were originally designed as "flight spares" for NIRCam (R. Doyon et al. 2023), they have very similar transmission curves. This enables us to check for any systematic biases in our flux measurements (e.g., from differing background subtraction, photometric calibrations, or segmentation) using the PASSAGE NIRISS and COSMOS-Web NIRCam fluxes in the F115W and F150W filters. We measure the fractional flux difference, $(f_{\rm COSMOS-Web} - f_{\rm PASSAGE})/f_{\rm COSMOS-Web}$, for crossmatched sources in F115W (F150W), finding a median offset of 1.5% (–0.7%) with a corresponding scatter of $\sigma = 22\%$ (18%). The scatter is higher than that observed in previous studies (e.g., P. J. Watson et al. 2025b), consistent with the lower median SNR in our catalog, but we are satisfied that there are no systematic variations between the two photometric datasets.

Stellar masses are derived following a similar procedure to that described in M. A. Malkan et al. (2025), summarized here. We model the stellar populations of each galaxy by fitting the photometry with the Bayesian Analysis of Galaxies for Physical Inference and Parameter EStimation (or BAGPIPES; A. C. Carnall et al. 2018)[34] SED-fitting code, using a seven-bin continuity star formation history prior (J. Leja et al. 2019). We fix the youngest age bin to 30 Myr and the oldest to 500 Myr below the age of the Universe at a given redshift, allowing both very young and maximally old populations. We allow the metallicity and ionization parameter to vary between (0.0, 3.0) $Z_\odot$ and (−3.5, −1.0), respectively. Dust attenuation is parameterized following D. Calzetti et al. (2000), allowing an A_V of up to 3 mag. The masses for AGN are expected to be highly unreliable, and we include an AGN flag in the catalog for sources identified as AGN in the COSMOS-Web DR1 release.

In the left panel of Figure 7, we present stellar masses as a function of redshift. The stellar masses span 10^6–$10^{11} M_\odot$. Point color corresponds to JWST/NIRCam F150W magnitude. The low-mass limit increases with redshift due to the decreasing apparent brightness of distant sources. We observe sources with masses below $10^7 M_\odot$ out to $z \sim 1.5$, and below $10^8 M_\odot$ out to $z \sim 3.3$, substantially exploring the mid- and low-mass galaxy population near and past cosmic noon.

In the middle panel of Figure 7, we compare PASSAGE-derived stellar masses (computed using COSMOS-Web photometry, additional NIRISS photometry, and fixed to PASSAGE $z_{\rm best}$) to masses derived using the `LePHARE` SED-fitting code (S. Arnouts et al. 2002; O. Ilbert et al. 2006) in the COSMOS-Web DR1 release. The color bar indicates the redshift discrepancy between PASSAGE and COSMOS-Web. We find that PASSAGE masses are, on average, larger than `LePHARE`-derived COSMOS-Web masses by ∼0.2 dex. In the right panel of Figure 7, we compare PASSAGE-derived stellar masses to those obtained using the `CIGALE` SED-fitting code (M. Boquien et al. 2019) in the COSMOS-Web DR1 release. In contrast to the `LePHARE`-derived masses, PASSAGE masses are typically ∼0.1 dex smaller than the `CIGALE`-derived COSMOS-Web masses. In both the `LePHARE` and `CIGALE` comparisons, the typical mass discrepancy is smaller than the scatter (the root mean squared error between the COSMOS-Web and PASSAGE masses is ∼0.3 dex in the `LePHARE` case and ∼0.5 dex in the `CIGALE` case). The dominant source of the mass discrepancy is the redshift difference between catalogs: When COSMOS-Web predicts a lower redshift for a source than PASSAGE, it also yields a lower stellar mass. The scatter between PASSAGE and COSMOS-Web masses is typically most pronounced at the low-mass end: For sources with COSMOS-Web $\log_{10}[M_*/M_\odot] \lesssim 7$ (for both the `LePHARE` and `CIGALE` cases), the corresponding PASSAGE stellar masses are typically larger by ∼1.4 dex. This low-mass discrepancy is primarily driven by the fact that these objects also typically have the most discrepant redshifts (where PASSAGE tends to predict higher redshifts than COSMOS-Web).

[34] https://bagpipes.readthedocs.io, version 1.3.2.

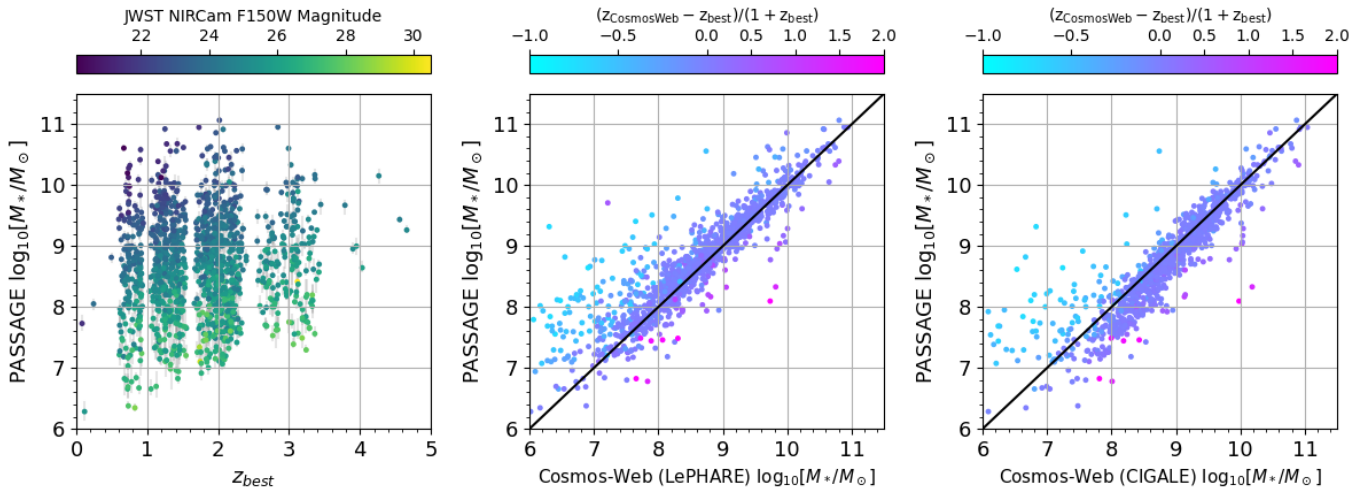

Figure 7. Left panel: stellar mass–redshift distribution for PASSAGE galaxies. The lower stellar-mass limit on PASSAGE observations increases with redshift, as lower-mass galaxies become more difficult to observe at larger distances. Middle panel: comparison between stellar masses derived in COSMOS-Web using LePHARE and those derived from PASSAGE. The color bar indicates the discrepancy between COSMOS-Web and PASSAGE redshifts. PASSAGE masses tend to be larger than COSMOS-Web masses derived with LePHARE, which correlates with higher PASSAGE redshifts. Right panel: same comparison as the middle panel, except using COSMOS-Web CIGALE-derived masses instead of LePHARE on the *x*-axis. PASSAGE masses tend to be smaller than COSMOS-Web masses derived with CIGALE. Error bars in the middle and right panels are omitted for clarity.

To test the effect of the NIRISS photometry, we rerun the SED fitting for Par028 without the NIRISS filters, while keeping the redshift fixed to $z_{\rm best}$. The resulting root mean squared error between Par028 PASSAGE masses with and without NIRISS photometry is 0.03 dex. For reference, we also rerun the SED fitting for Par028 including NIRISS filters but adopting $z_{\rm COSMOSWeb}$ instead of $z_{\rm best}$. This gives a root mean squared error of 0.38 dex, demonstrating that redshift differences have a substantially larger impact on stellar-mass estimates than the inclusion of additional photometry.

8. Conclusion

We present a spectroscopic redshift catalog of 2183 galaxies spanning $0.08 < z < 4.7$ from 15 PASSAGE fields in the COSMOS region. We describe the emission-line identification pipeline and visual inspection procedure, which together mitigate contamination and assign reliability flags to each source, with lower flag values indicating higher-confidence redshifts.

Of the 2183 emission-line sources, 1955 previously lacked spectroscopic redshift measurements. Crossmatching with COSMOS photometric catalogs shows strong agreement between PASSAGE spectroscopic redshifts and photometric redshifts for the most robust (flag 1) sources, with increasing scatter toward higher flag values. For the lowest-confidence redshifts (flag 4), we find that single-line Hα emitters are misidentified at the $\sim$19% level. Using COSMOS photometric information, we confirm or refine the redshifts of a subset of these sources. We also find excellent agreement between PASSAGE redshifts and existing spectroscopic measurements from the A. A. Khostovan et al. (2026) compilation.

For sources within the COSMOS-Web footprint, we derive stellar masses and show that PASSAGE probes the low- and intermediate-mass galaxy population, reaching $\log_{10}(M_*/M_\odot) \lesssim 8$ out to $z \sim 3.3$. PASSAGE-derived stellar masses are systematically offset relative to COSMOS-Web estimates derived with LEPHARE and CIGALE, with differences primarily driven by redshift discrepancies.

The methodology and results presented here have important implications for the broader PASSAGE survey. The remaining 48 PASSAGE fields lack uniform ancillary photometry, and the limitations identified for spectroscopic redshifts—particularly for single-line emitters—must be accounted for in future analyses. Ongoing follow-up efforts, including HST-SNAP, Very Large Telescope FORS2, and Keck observations, will provide critical photometric constraints to improve redshift assignments and enable stellar-mass measurements in fields without existing ancillary data. More generally, this work highlights the value of incorporating photometric information when interpreting single-line slitless spectra, a lesson applicable to other pure-parallel surveys such as POPPIES (J. Kartaltepe et al. 2024) and SAPPHIRES (E. Egami et al. 2024).

Finally, this catalog provides an important reference dataset for upcoming Euclid and Roman spectroscopy, both of which will observe the COSMOS field. The PASSAGE redshift sample will enable cross-comparisons and consistency checks with Euclid and Roman measurements, while future spectroscopy from these missions will further test and refine PASSAGE redshifts, particularly for lower-confidence sources. Such cross-validation will be especially valuable given that approximately 44% of the full PASSAGE survey consists of fields with single-filter spectroscopy.

Acknowledgments

This research was supported by the International Space Science Institute (ISSI) in Bern, through ISSI International Team project #24-624. This work was supported by NASA through grant No. JWST-GO-1571. All the JWST data used in this paper can be found in MAST (doi:10.17909/6ca5-ba17). A.A., B.V., and P.J.W. acknowledge support from the European Union – NextGenerationEU RFF M4C2 1.1 PRIN 2022 project 2022ZSL4BL INSIGHT. P.J.W. and B.V. acknowledge support from the INAF Mini Grant "1.05.24.07.01 RSN1: Spatially Resolved Near-IR Emission of Intermediate-Redshift Jellyfish Galaxies" (PI: Watson). A.J.B. acknowledges funding from the

"FirstGalaxies" Advanced Grant from the European Research Council (ERC) under the European Union's Horizon 2020 research and innovation program (grant agreement No. 789056).

Software: NumPy (C. R. Harris et al. 2020), SciPy (P. Virtanen et al. 2020), AstroPy (Astropy Collaboration et al. 2013, 2018, 2022), Matplotlib (J. D. Hunter 2007), GRIZLI (G. Brammer & J. Matharu 2021), SEP (E. Bertin & S. Arnouts 1996; K. Barbary 2016).

Appendix A
Emission Lines in the Line-finder Interface

Table 4 lists all emission lines included in the line-finder interface to assist with visual identification.

Table 4
Lines Considered during the Line-finding Visual Inspection Effort

Emission Line	Vacuum Wavelength (Å)
Lyα	1215.67
N V	1238.82, 1242.80
C IV	1548.20, 1550.78
He II	1640.42
O III	1660.81
Si III]	1892.03
C III]	1908.73
Mg II	2796.35, 2803.53
[O II]	3727.09, 3729.88
[Ne III]	3869.88, 3968.64
Hϵ	3971.19
Hδ	4102.89
Hγ	4341.68
[O III]	4364.44
He II	4687.02
Hβ	4862.68
[O III]	4960.30, 5008.24
He I	5877.25
[O I]	6365.54
Hα	6564.61
[S II]	6718.29, 6732.67
[S III]	9071.10, 9533.20
He I	10832.9
Paγ	10941.1
Paβ	12821.6
Paα	18756.1

Appendix B
Off-center Emission

One additional challenge in assigning spectroscopic redshifts is the presence of off-center emission. Clumpy star formation, galaxy mergers, accretion, and outflows can produce emission peaks that do not correspond to the host galaxy's photometric center. An example of a source with substantial off-center emission is seen in Figure 8. Two bright clumps can be seen in the F150W direct image, which translates to two distinct peaks for each emission line in both the 1D and 2D spectra. The two pairs of peaks likely correspond to Hα and [O III], but the spectroscopic redshift is likely inexact. If we assume the left peaks of each pair of emission-line peaks are the observed wavelengths of Hα and [O III] (as shown in Figure 8), $z_{\rm spec} = 1.1863$. If we instead assume the right peaks of each pair of emission-line peaks are the observed wavelengths of Hα and [O III], $z_{\rm spec} = 1.2693$. It is most likely that neither of these redshifts best represent the true $z_{\rm spec}$ of the source, and rather the true $z_{\rm spec}$ lies somewhere between the two sets of emission lines. While such off-center emission cases are relatively rare, they are expected to become increasingly common in upcoming Euclid and Roman spectroscopy. Disentangling these off-center features and obtaining reliable redshifts will require observations where the traces are dispersed at multiple orientations or roll angles.

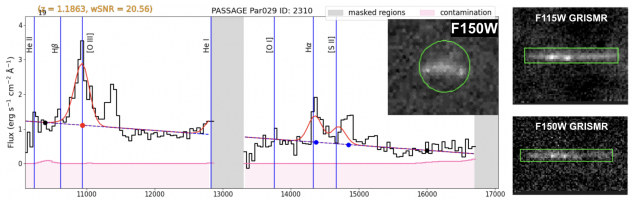

Figure 8. Example of a PASSAGE source with off-center emission in Par029, shown with F150W imaging (center insert) and F115W and F150W GRISMR spectra (right panels). The assigned spectroscopic redshift of the source varies depending on which set of emission peaks is assigned to Hα and [O III], emphasizing the challenge of determining redshifts for sources with off-center emission. In the 1D spectra, the emission lines are aligned with the left set of peaks for Hα and [O III], which is likely offset from the true spectroscopic redshift.

Appendix C
Expanded Comparison to A. A. Khostovan et al. (2026)

In Section 5.2, we compared PASSAGE spectroscopic redshifts with the A. A. Khostovan et al. (2026) spectroscopic redshift compilation for sources with high-quality flags in both samples. Here, we expand this comparison to all 228 crossmatched sources between the catalogs, regardless of quality flag. This comparison is shown in the left panel of Figure 9.

A total of 168 of the 228 sources (74%) agree within $|z_{\rm Khostovan+} - z_{\rm best}| < 0.1$, indicating that even when including lower-quality redshifts, the two catalogs remain in relatively strong agreement. This agreement drops from 74% to 61% when excluding the high-quality redshift sources in both catalogs (included in the comparison in Figure 4), indicating that even for low-quality redshifts, PASSAGE and A. A. Khostovan et al. (2026) still agree for a majority of cases. Of the 60 sources with $|z_{\rm Khostovan+} - z_{\rm best}| > 0.1$, 37 are PASSAGE flag 1 (robust) sources. For example, the source with $z_{\rm best} = 2.05113$ and $z_{\rm Khostovan+} = 0.28777$ (shown in the right panel of Figure 9) has a highly robust PASSAGE

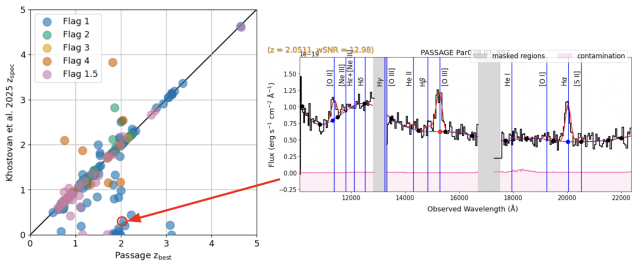

Figure 9. Left panel: same as Figure 4, except all spectroscopic redshifts from A. A. Khostovan et al. (2026) and PASSAGE (regardless of quality flag) are included in the comparison. Right panel: an example source where PASSAGE provides a more accurate spectroscopic redshift than was previously available.

redshift, constrained primarily by the Hα, [O III], and [O II] lines. In the A. A. Khostovan et al. (2026) compilation, however, it is assigned a "tentative" redshift measurement $Q_f = 1$ (50% confidence), meaning their spectroscopic redshift is very poorly constrained. The photometric $z_{\rm COSMOS\text{-}Web} = 1.95^{+0.08}_{-2.05}$ for this source agrees better with the PASSAGE $z_{\rm best}$ than $z_{\rm Khostovan+}$. This again emphasizes the importance of the PASSAGE sample: Not only does it substantially add to the existing sample of spectroscopic redshifts, but it can also increase the robustness of (and even correct) existing spectroscopic redshifts.

ORCID iDs

Mason S. Huberty https://orcid.org/0009-0002-9932-4461
Kalina V. Nedkova https://orcid.org/0000-0001-5294-8002
Zahra Sattari https://orcid.org/0000-0002-0364-1159
Vihang Mehta https://orcid.org/0000-0001-7166-6035
Claudia Scarlata https://orcid.org/0000-0002-9136-8876
Marc Rafelski https://orcid.org/0000-0002-9946-4731
Matthew J. Hayes https://orcid.org/0000-0001-8587-218X
Peter J. Watson https://orcid.org/0000-0003-3108-0624
Ayan Acharyya https://orcid.org/0000-0003-4804-7142
Jacob Levine https://orcid.org/0009-0000-9478-1933
Benedetta Vulcani https://orcid.org/0000-0003-0980-1499
Alexandra Le Reste https://orcid.org/0000-0003-1767-6421
Farhanul Hasan https://orcid.org/0000-0002-0072-0281
James Colbert https://orcid.org/0000-0001-6482-3020
Michele Trenti https://orcid.org/0000-0001-9391-305X
Xin Wang https://orcid.org/0000-0002-9373-3865
Axel Runnholm https://orcid.org/0000-0002-1025-7569
Matthew A. Malkan https://orcid.org/0000-0001-6919-1237
Andrew J. Bunker https://orcid.org/0000-0002-8651-9879
Anahita Alavi https://orcid.org/0000-0002-8630-6435
Hakim Atek https://orcid.org/0000-0002-7570-0824
Andrew J. Battisti https://orcid.org/0000-0003-4569-2285
Y. Sophia Dai https://orcid.org/0000-0002-7928-416X
Keunho Kim https://orcid.org/0000-0001-6505-0293
Alaina Henry https://orcid.org/0000-0002-6586-4446
Michael J. Rutkowski https://orcid.org/0000-0001-7016-5220
Hollis Akins https://orcid.org/0000-0003-3596-8794
Caitlin M. Casey https://orcid.org/0000-0002-0930-6466
Maximilien Franco https://orcid.org/0000-0002-3560-8599
Santosh Harish https://orcid.org/0000-0003-0129-2079
Jeyhan S. Kartaltepe https://orcid.org/0000-0001-9187-3605
Anton Koekemoer https://orcid.org/0000-0002-6610-2048
Daizhong Liu https://orcid.org/0000-0001-9773-7479
Henry McCracken https://orcid.org/0000-0002-9489-7765
Jason Rhodes https://orcid.org/0000-0002-4485-8549
Brant Robertson https://orcid.org/0000-0002-4271-0364
Marko Shuntov https://orcid.org/0000-0002-7087-0701

References

Acharyya, A., Watson, P. J., Vulcani, B., et al. 2025, arXiv:2508.05335
Aihara, H., AlSayyad, Y., Ando, M., et al. 2019, PASJ, 71, 114
Arnouts, S., Moscardini, L., Vanzella, E., et al. 2002, MNRAS, 329, 355
Astropy Collaboration, Price-Whelan, A. M., Lim, P. L., et al. 2022, ApJ, 935, 167
Astropy Collaboration, Price-Whelan, A. M., Sipőcz, B. M., et al. 2018, AJ, 156, 123
Astropy Collaboration, Robitaille, T. P., Tollerud, E. J., et al. 2013, A&A, 558, A33
Barbary, K. 2016, JOSS, 1, 58
Baronchelli, I., Scarlata, C. M., Rodighiero, G., et al. 2020, ApJS, 249, 12
Baronchelli, I., Scarlata, C. M., Rodríguez-Muñoz, L., et al. 2021, ApJS, 257, 67
Battisti, A. J., Bagley, M. B., Rafelski, M., et al. 2024, MNRAS, 530, 894
Bertin, E., & Arnouts, S. 1996, A&AS, 117, 393
Bertin, E., Schefer, M., Apostolakos, N., et al. 2020, ASPC, 527, 461
Boquien, M., Burgarella, D., Roehlly, Y., et al. 2019, A&A, 622, A103
Boyett, K., Bunker, A. J., Chevallard, J., et al. 2024, MNRAS, 534, 814
Brammer, G., & Matharu, J. 2021, gbrammer/grizli: Release 2021, v1.3.2, Zenodo, doi:10.5281/zenodo.5012699
Brammer, G. B., van Dokkum, P. G., & Coppi, P. 2008, ApJ, 686, 1503
Calzetti, D., Armus, L., Bohlin, R. C., et al. 2000, ApJ, 533, 682
Capak, P., Aussel, H., Ajiki, M., et al. 2007, ApJS, 172, 99
Carnall, A. C., McLure, R. J., Dunlop, J. S., & Davé, R. 2018, MNRAS, 480, 4379
Casey, C. M., Kartaltepe, J. S., Drakos, N. E., et al. 2023, ApJ, 954, 31
Colbert, J. W., Teplitz, H., Atek, H., et al. 2013, ApJ, 779, 34
Doyon, R., Willott, C. J., Hutchings, J. B., et al. 2023, PASP, 135, 098001
Du, P., Kibbe, W. A., & Lin, S. M. 2006, Bioin, 22, 2059
Egami, E., Fan, X., Sun, F., et al. 2024, JWST Proposal, Cycle 3, 6434
Estrada-Carpenter, V., Sawicki, M., Abraham, R., et al. 2025, ApJ, 991, 188
Finkelstein, S. L., Bagley, M. B., Arrabal Haro, P., et al. 2025, ApJL, 983, L4
Franco, M., Casey, C. M., Koekemoer, A. M., et al. 2026, ApJ, 999, 200
Harris, C. R., Millman, K. J., van der Walt, S. J., et al. 2020, Natur, 585, 357
Hoaglin, D. C., Mosteller, F., & Tukey, J. W. 1983, Understanding Robust and Exploratory Data Analysis (Wiley)
Hunter, J. D. 2007, CSE, 9, 90
Ilbert, O., Arnouts, S., McCracken, H. J., et al. 2006, A&A, 457, 841
Kakiichi, K., Egami, E., Fan, X., et al. 2024, JWST Proposal, Cycle 3, 5893
Kartaltepe, J., Rafelski, M., Alavi, A., et al. 2024, JWST Proposal, Cycle 3, 5398
Kashino, D., Lilly, S. J., Matthee, J., et al. 2023, ApJ, 950, 66
Khostovan, A. A., Kartaltepe, J. S., Salvato, M., et al. 2026, ApJS, 282, 6
Koekemoer, A. M., Aussel, H., Calzetti, D., et al. 2007, ApJS, 172, 196
Kümmel, M., Álvarez-Ayllón, A., Bertin, E., et al. 2022, arXiv:2212.02428
Leja, J., Carnall, A. C., Johnson, B. D., Conroy, C., & Speagle, J. S. 2019, ApJ, 876, 3
Malkan, M. A., Mehta, V., Acharyya, A., et al. 2025, ApJ, 993, 152
Massey, R., Stoughton, C., Leauthaud, A., et al. 2010, MNRAS, 401, 371
McCracken, H. J., Milvang-Jensen, B., Dunlop, J., et al. 2012, A&A, 544, A156
Nedkova, K., Henry, A., Rafelski, M., & Revalski, M. 2026, Line Finding Software for NIRISS Slitless Spectroscopy, v1.0.0, Zenodo, doi:10.5281/zenodo.19228845
Noirot, G., Desprez, G., Asada, Y., et al. 2023, MNRAS, 525, 1867
Oesch, P. A., Brammer, G., Naidu, R. P., et al. 2023, MNRAS, 525, 2864
Oke, J. B., & Gunn, J. E. 1983, ApJ, 266, 713
Ratajczak, J., Dawson, K. S., Weaverdyck, N., et al. 2026, AJ, 171, 71
Revalski, M., Rafelski, M., Henry, A., et al. 2024, ApJ, 966, 228
Runnholm, A., Hayes, M. J., Mehta, V., et al. 2025, ApJ, 984, 95
Sanders, D. B., Salvato, M., Aussel, H., et al. 2007, ApJS, 172, 86
Sarrouh, G. T. E., Asada, Y., Martis, N. S., et al. 2026, ApJS, 282, 3
Sawicki, M., Arnouts, S., Huang, J., et al. 2019, MNRAS, 489, 5202
Scoville, N., Aussel, H., Brusa, M., et al. 2007, ApJS, 172
Shuntov, M., Akins, H. B., Paquereau, L., et al. 2025, A&A, 704, A339
Storey, P. J., & Zeippen, C. J. 2000, MNRAS, 312, 813
Taniguchi, Y., Kajisawa, M., Kobayashi, M. A. R., et al. 2015, PASJ, 67, 104
Treu, T., Roberts-Borsani, G., Bradac, M., et al. 2022, ApJ, 935, 110
Virtanen, P., Gommers, R., Oliphant, T. E., et al. 2020, NatMe, 17, 261
Wang, B., Leja, J., Labbé, I., et al. 2024, ApJS, 270, 12
Watson, P. J., Vulcani, B., Treu, T., et al. 2025a, A&A, 699, A225
Watson, P. J., Vulcani, B., Werle, A., et al. 2025b, A&A, 699, A365
Weaver, J. R., Kauffmann, O. B., Ilbert, O., et al. 2022, ApJS, 258, 11
Willott, C. J., Doyon, R., Albert, L., et al. 2022, PASP, 134, 025002